



**AFM-PATTERNED 2-D THIN-FILM PHOTONIC CRYSTAL ANALYZED BY  
COMPLETE ANGLE SCATTER**

THESIS

Nicholas C. Herr, 2<sup>nd</sup> Lieutenant, USAF

AFIT/GMS/ENP/10-M01

**DEPARTMENT OF THE AIR FORCE  
AIR UNIVERSITY**

**AIR FORCE INSTITUTE OF TECHNOLOGY**

---

---

**Wright-Patterson Air Force Base, Ohio**

APPROVED FOR PUBLIC RELEASE; DISTRIBUTION UNLIMITED

The views expressed in this thesis are those of the author and do not reflect the official policy or position of the United States Air Force, Department of Defense, or the United States Government.

AFIT/GMS/ENP/10-M01

AFM-PATTERNED 2-D THIN-FILM PHOTONIC CRYSTAL ANALYZED BY  
COMPLETE ANGLE SCATTER

THESIS

Presented to the Faculty

Department of Engineering Physics

Graduate School of Engineering and Management

Air Force Institute of Technology

Air University

Air Education and Training Command

In Partial Fulfillment of the Requirements for the

Degree of Master of Science in Materials Science

Nicholas C. Herr, BSMS

2<sup>nd</sup> Lieutenant, USAF

March 2010

APPROVED FOR PUBLIC RELEASE; DISTRIBUTION UNLIMITED

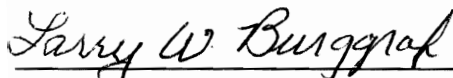
AFIT/GMS/ENP/10-M01

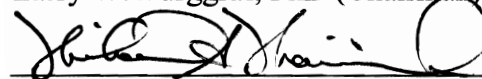
AFM-PATTERNED 2-D THIN-FILM PHOTONIC CRYSTAL ANALYZED BY  
COMPLETE ANGLE SCATTER

Nicholas C. Herr, BSMS

2<sup>nd</sup> Lieutenant, USAF

Approved:

  
\_\_\_\_\_  
Larry W. Burggraf, PhD (Chairman)

  
\_\_\_\_\_  
Michael A. Marciniak, PhD (Member)

  
\_\_\_\_\_  
Alex G. Li, PhD (Member)

17 Mar 2010  
Date

17 Mar 10  
Date

17 Mar 2010  
Date

### **Abstract**

The purpose of this research was to use an atomic force microscope (AFM) to generate a 2-D square array of sub-wavelength surface features from a single material over a region large enough to permit optical characterization. This work is an extension of previous AFIT nano-patterning work and is in response to the small subunit sizes demanded for the production of optical metamaterials and photonic crystals. A diamond nano-indentation AFM probe was used to produce a 325- $\mu\text{m}$  by 200- $\mu\text{m}$  array of indentations in a 120-nm thick polystyrene film deposited on silicon. Indentation spacing of 400 nm produced well-defined surface features with a maximum height of 140 nm. The full size array was achieved by tiling together single arrays, limited in size by the AFM scanner range, through the use of the AFM's translation stage. A Complete Angle Scatter Instrument (CASI) was used (beam focused to 140  $\mu\text{m}$ ) to determine scatter at incident angles ranging from 0 to 80 degrees. Two wavelengths were investigated (633 and 544 nm) at both s and p-polarization. Negative first order diffraction peaks were observed for both wavelengths and were consistent with feature spacing. This is the first demonstration of an AFM-patterned surface to behave as a 2D photonic crystal and has potential DoD applications in laser eye protection, enhanced solar cell efficiency, satellite thermal management, and anti-reflection coatings for high power laser optics.

## **Acknowledgments**

I would like to thank my wife for her love and support during this endeavor. I would also like to express my sincere appreciation to my advisor, Dr. Larry Burggraf, for his guidance throughout the project and to the other members of my committee, Dr. Alex Li and Dr. Michael Marciniak, for their active involvement during various stages of my work. Thanks are also due to Mr. Dominic Maga for his assistance in CASI data collection and 2<sup>nd</sup> Lt Shawn Hackett for his programming assistance. And above all, I would like to thank Almighty God.

Nicholas C. Herr

## Table of Contents

	Page
Abstract .....	iv
Acknowledgments .....	v
Table of Contents .....	vi
List of Figures .....	viii
 I. Introduction .....	 1
Photonic Crystals (PC) .....	2
Negative Index Metamaterials (NIM) .....	2
Atomic Force Microscope (AFM) Surface Modification .....	5
Optical Characterization of Photonic Crystals and Metamaterials .....	6
Problem Statement .....	7
Research Objectives .....	7
Research Impact .....	8
Methodology .....	8
 II. Atomic Force Microscope (AFM) .....	 10
Overview .....	10
Basic Operation .....	10
AFM Instrumentation and Components .....	11
AFM Software Operating Parameters .....	14
Ramping Parameters .....	19
Summary .....	21
 III. Sample Production .....	 22
Chapter Overview .....	22
Substrate Preparation .....	22
Force Modulation (FM) .....	24
Ringing Oscillations .....	26
Nano-indentation with Diamond AFM Tip .....	30
Summary .....	41
 IV. Complete Angle Scatter Instrument (CASI) .....	 42
Chapter Overview .....	42
Complete Angle Scatter Instrument (CASI) System .....	42
Normal CASI Operation .....	44

	Page
Focused CASI Beam .....	45
Summary.....	47
V. CASI Results .....	48
Chapter Overview.....	48
CASI Measurements.....	48
Patterned Sample - 633 nm.....	57
Patterned Sample – 544 nm.....	61
Investigative Questions Answered .....	64
Summary.....	65
VI. Conclusions and Recommendations.....	66
Chapter Overview.....	66
Contributions of Research .....	66
Significance of Research .....	67
Recommendations for Action.....	67
Recommendations for Future Research.....	69
Summary.....	69
Appendix A.....	70
Appendix B .....	72
Bibliography .....	73



## List of Figures

Figure	Page
1: Atomic Force Microscope (AFM) diagram [25] .....	11
2: Dimension V SPM system.....	11
3: Dimension V SPM with schematic tracing laser path inside scanner head. ....	12
4: Relationship between scan size and X/Y offset.....	18
5: Illustration of ramp size and Z scan start.....	20
6: AFM image of the surface scratch, including cross section showing its depth (120 nm) .....	23
7: Polystyrene film on silicon substrate, arrow showing approximate location of patterned area .....	24
8: (a) FM ringing patterning (b) faint ringing FM patterns .....	26
9: (a) Patterning with ringing oscillations and (b) image of resulting pattern .....	29
10: Completed AFM-patterned 2-D thin-film photonic crystal (each pattern is numbered in lower left corner in the order they were produced).....	30
11: AFM image of the patterned surface .....	31
12: 5 x 5 Nano-indentation trial arrays showing indentation consistency and the effect of feature spacing. ....	33
13: 20 x 20 nano-indentation array, 400 nm spacing.....	34
14: Example of reduced Y scanner range. ....	35
15: Automatic initial Z scan start value when entering ramp mode. ....	40
16: CASI source box [22]. ....	43

Figure	Page
17: Sample mount (AFM-patterned sample) .....	44
18: Focused CASI laser configuration (on patterned sample) .....	46
19: Magnification apparatus for centering CASI laser on patterned area .....	47
20: 10 $\mu\text{m}$ AFM calibration standard (AFM image) .....	49
21: (a) Comparison between CASI laser focused at detector and sample, 10 $\mu\text{m}$ AFM standard, $\theta_i = 40^\circ$ , p-polarization, 633 nm (b) zoomed in .....	50
22: (a) Comparison between CASI laser focused at detector and sample, 10 $\mu\text{m}$ AFM standard, $\theta_i = 40^\circ$ , p-polarization, 544 nm (b) zoomed in .....	51
23: (a) Comparison between s-and p-polarization, 10- $\mu\text{m}$ AFM standard, $\theta_i = 40^\circ$ , p- polarization, 544 nm, focused at sample (b) zoomed in .....	53
24: Fit between diffraction angles predicted by grating equation and experimentally obtained diffraction angles (at corresponding diffraction orders) for 10- $\mu\text{m}$ AFM standard grid, p-polarization (focused at detector) at $\theta_i = 40^\circ$ for 633 nm (red) and 544 nm (green). .....	54
25: Un-patterned polystyrene control, $\theta_i = 40^\circ$ , 633 nm. ....	55
26: 3-D plot of $\text{Log}_{10}[\text{BRDF}]$ vs. $\theta_i$ and $\theta_r$ for the polystyrene surface, 633 nm. ....	56
27: 3-D plot of $\text{Log}_{10}[\text{BRDF}]$ vs. $\theta_i$ and $\theta_r$ for the patterned sample, 633 nm, long axis of pattern parallel to incoming laser .....	58
28: Fit between $m=-1$ diffraction order at different $\theta_i$ predicted by grating equation $(m\lambda = d(\sin \theta_r - \sin \theta_i))$ and experimentally obtained diffraction angles for patterned sample, p-polarization, 633 nm. ....	59

Figure	Page
29: Diffraction pattern for AFM-patterned sample.....	59
30: Patterned polystyrene, $\theta_i = 40^\circ$ , showing expanded view of additional feature at 70.27°, normal pattern orientation only, both polarizations, 633 nm. ....	60
31: Patterned polystyrene, $\theta_i = 40^\circ$ , showing expanded view of additional feature at 70.27°, both pattern orientations, both polarizations, 633 nm. ....	61
32: 3-D plot of $\text{Log}_{10}[\text{BRDF}]$ vs. $\theta_i$ and $\theta_r$ for the patterned sample, 544 nm, long axis of pattern parallel to incoming laser .....	62
33: Patterned polystyrene, $\theta_i = 60^\circ$ , showing additional feature at 28.8°, both polarizations, 544 nm. ....	63
34: Patterned polystyrene, $\theta_i = 60^\circ$ , showing additional feature at 28.8°, both pattern orientations, both polarizations, 544 nm. ....	64

# AFM-PATTERNED 2-D THIN-FILM PHOTONIC CRYSTAL ANALYZED BY COMPLETE ANGLE SCATTER

## I. Introduction

World-changing technological breakthroughs typically occur when new material properties are more thoroughly understood and made controllable. Understanding and controlling the mechanical properties of materials made our high-speed, high-rise and high-flying world possible. Understanding and controlling the electrical properties of materials has enabled the current electronic revolution. In the same way, emerging understanding of and control over the optical properties of materials will usher in the next revolution. In coming decades, optical materials (photonic crystals) that prohibit, direct, and localize light propagation will become more developed and more prevalent [1]. Control over optical properties is also being extended to include the creation of new optical properties (metamaterials) and may permit the development of truly amazing future devices. In the near term, potential DoD applications exist in laser eye protection [2-4], enhanced solar cell efficiency [5], satellite thermal management [6], and anti-reflection coatings for high power laser optics.

However, increases in the ability to control material properties require corresponding increases in the careful production of those materials. Controlling mechanical properties requires control over *macroscopic* material composition and processing. Electronic property control requires control over *microscopic* material

composition and processing. Control of optical properties requires *nanoscopic* control over not only material composition but also material construction. Exercising this level of control makes great demands on current fabrication techniques and is a primary difficulty in the further development of these optical materials [7]. This is complicated further by the demand that for many practical applications these nanoscopic structures will need to be produced in sizes approaching a meter (or more).

### **Photonic Crystals (PC)**

The defining feature of a photonic crystal is its periodic variation in refractive index. This periodicity can be in one, two, or three dimensions within the crystal and can range in size from nanometers to centimeters. The utility of this periodic index arises when the scale of the periodicity is similar to that of incoming light. Under these conditions, Maxwell's equations and the crystalline periodic boundary conditions predict that the propagation of light can be completely inhibited, producing a photonic band gap (PBG) similar to the electronic band gap of semiconductors. Introducing defects into the PC disrupts the PBG and allows inhibited light to flow along certain paths. These paths may be within an optical integrated circuit (optical computing) or down the center of a PC fiber (optical data transfer) [8].

### **Negative Index Metamaterials (NIM)**

Metamaterials derive their properties from their periodic structure as well. However, the subunits that make up metamaterials are much smaller than the incoming light. This allows a metamaterial to be described by the same electromagnetic (EM)

parameters that describe normal materials: the electric permittivity,  $\epsilon$ , and  $\mu$ , the magnetic permeability. For traditional transparent optical materials (glass), both these parameters are positive and together give the material a real, positive value for the refractive index ( $n = \sqrt{\epsilon} \sqrt{\mu}$ ). In a metamaterial, the tiny subunits that give rise to  $\epsilon$  and  $\mu$  are very carefully designed and constructed to produce negative values for both these constants over certain wavelength ranges. Because their product is positive, the refractive index is still a real value and the material is transparent.

The transparency of metamaterials is where their similarities to traditional optical materials generally end. In fact, metamaterials behave differently with respect to many well-known optical phenomena. The frequency shift they experience due to the Doppler effect is reversed, as is the direction of their Cherenkov radiation emission. These both flow from the fact that the group and phase velocities in a metamaterial point in the opposite direction (rather than being parallel). It also gives rise to a metamaterial's most intriguing new property – the negative sign of the refractive index.

The negative refractive index of metamaterials has several powerful potential applications. For example, a lens with a negative index focuses incoming light very differently than an ordinary lens. It focuses ordinary propagating light rays like an ordinary lens, but it also focuses and amplifies the evanescent waves that normally decay away. These evanescent waves contain additional information about an object and allow imaging at high spatial resolution using a smaller optical device to be realized, limited only by the quality of the metamaterial [9].

Another potential application made possible by the ability to control the electromagnetic material properties of metamaterials is cloaking (invisibility). In metamaterial cloaking, the basic idea is to construct a metamaterial layer designed to bend light around an object. The light emerges just as it would have had it not encountered the cloak at all, rendering the object invisible. Though this sounds like science fiction, working devices have already been constructed at microwave and proposed for optical wavelengths [10-13].

The applications of PCs and NIMs are very exciting. However, manufacturing these materials at the nanometer scales required for them to operate at optical wavelengths is difficult and expensive. The current method of choice is electron-beam lithography (EBL), though it suffers from long writing times and high cost. These constraints have spurred the development of alternative methods such as interference and nanoimprint lithography [14-15].

This work aims to address the deficiencies of long writing times and high cost as well through the use of stress-induced surface nano-patterning. The AFM techniques used here are only a demonstration of surface nano-patterning. More practical nano-patterning would require the development of 1D knife edges or combs used in place of the AFM tip or the development of a template-driven technique utilizing force (as in this work) or elevated temperatures for surface patterning. In these instances, the AFM would be a useful tool for quality control and for the generation of a master template. In both instances, as well as in current EBL techniques, the 2D surface structures that are

produced would require sequential layering before the materials produced would be suitable for potential applications.

### **Atomic Force Microscope (AFM) Surface Modification**

Atomic force microscopy (AFM) was conceived and is most commonly used as an imaging technique. In AFM, a sharp tip is scanned over a surface and the resulting forces are interpreted to create a topographic image of the surface at nanometer scales. However, as it has developed, AFM has been increasingly used to re-shape and construct surfaces in addition to merely imaging them. Some techniques carefully control the interaction between a sharp tip and surface atoms to move atoms around or to pick them up and deposit them elsewhere [16]. Other techniques use the AFM tip to carefully control surface chemical reactions (nano-lithography) [17-18]. It has also been well demonstrated that under appropriate operating conditions, an AFM tip can create structures from a single material [19-22] by the application of surface stress.

Surface stress can be applied to a material by an AFM tip in several ways. The simplest is to scan an AFM tip in contact with the surface at a high normal force. Under these conditions, on a soft material like polystyrene, scanning will produce parallel ridges oriented perpendicular to the scan direction. A slightly more complicated method for introducing surface stress is to modulate the motion of the AFM tip, effectively turning it into a nano-hammer [23-25]. If delivered in phase, the nano-hammer “strikes” reinforce each other and produce parallel ridges as well, but controlling the period of the modulation permits ridge spacing control. The most successful method demonstrated to produce in-phase tip modulation involves tuning the AFM feedback control parameters to



induce ‘ringing’ tip oscillations [23-25]. However, any AFM mode capable of exciting periodic tip oscillations can potentially be used to reshape a surface. Once surface ridges are produced it is a simple matter to rotate the scan angle and repeat the process to generate a second set of ridges. Superposition of the two sets of ridges gives rise to more complex two-dimensional surface structures. The symmetry of the resulting pattern is controlled by the relative angle between the two scan directions [25].

Surface stress can also be applied without scanning the tip at all. Instead, the tip is held stationary and simply pressed into the material. If the surface is soft enough and the tip is hard enough, a lasting indentation will be created in the surface. Depending on the shape of the tip and the interval at which indentations are made, a pattern of surface features can result.

### **Optical Characterization of Photonic Crystals and Metamaterials**

Regardless of how a photonic crystal or metamaterial is produced, whether by EBL or another method, it must be tested to ensure the desired EM properties are actually present. Experimental verification is commonly done using a system wherein EM radiation is directed at the sample and a rotating detector arm is used to collect the resulting scatter. This basic technique was used to defend the validity of NIMs against early challenges [26-27]. It has been used at this institution (AFIT) to characterize the scatter from photonic crystals using a Complete Angle Scatter Instrument (CASI) [4]. Ongoing work is also being conducted to develop a CASI-based Bidirectional Ellipsometry (BE) technique for more advanced metamaterial characterization [28].

## **Problem Statement**

Both photonic crystals and negative index metamaterials require that the periodic features that comprise them be smaller than a wavelength. Fabricating at this small scale in the optical regime is challenging, as is scaling up production over larger areas. Because of this, the size of metamaterial samples is usually small. This complicates optical characterization. This work means to address both of these problems.

## **Research Objectives**

Successful prior AFM nano-patterning work utilized ringing feedback oscillations to turn the AFM tip into a nano-hammer. This work was completed on a small, bench-top AFM and surface patterns were limited to a few microns in size [24-25]. The first objective of this work was to replicate previous nano-patterning results on a newer AFM model (Dimension V) for a single nano-patterned array. The next objective was to use the translation stage of the Dimension V to generate multiple individual arrays in a secondary two dimensional array, similar to a tiled floor. Patterning was continued as long as possible to generate a pattern covering as large an area as possible.

Once completed, the AFM-patterned sample was removed from the AFM and scattering measurements were conducted with the Complete Angle Scatter Instrument (CASI). Modifications were necessary to reduce the laser spot size of the CASI to prevent the sample from being overfilled. Two wavelengths were investigated – 633 and 544 nm.

## **Research Impact**

PCs and NIMs together represent exciting new advances in optical materials and offer the potential of amazing new capabilities. However, their wide-spread use requires that an alternative to the costly fabrication techniques currently used in their production be developed. AFM nano-patterning has the potential to generate surface features on the nanometer scale required. It offers the ability to easily adjust surface feature spacing. Appropriately configured, it has the potential to generate surface features quickly and on a variety of materials.

Demonstrating optical characterization of the AFM-generated nano-pattern will add to the growing body of work characterizing PCs and NIMs via optical scattering. CASI modifications required to permit scattering experiments on small samples will enable future experiments of this type to be conducted.

## **Methodology**

As previously stated, the first objective of this work was to replicate previous nano-patterning results [24-25] on an AFM model with a larger scanner range and motorized translation stage (Dimension V). Three techniques were used to do this. Two techniques made use of an oscillating nano-hammer tip – one by inducing ringing oscillations, the other by using a specialized Force Modulation (FM) AFM cantilever holder. The third technique made use of a native Dimension V operating mode (ramping mode) to create a 2-D array of nano-indentations.

Once high-quality nano-patterns were generated consistently (ramping mode), efforts were focused on generating the largest single nano-pattern possible. The limiting factor was the range of the AFM scanner.

The next step was to generate many nano-patterns in a secondary two-dimensional array, using a tiling approach. This was done by withdrawing the AFM tip, translating the sample stage and re-engaging the tip in the location of the new pattern. The goal was to produce a patterned area large enough to accommodate the laser spot size of the CASI. The patterned area required was greatly reduced by focusing the CASI laser to 140  $\mu\text{m}$  in diameter by suspending an additional 500 mm focal length lens between the laser source and the sample.

The next step was to analyze the scattering characteristics of the patterned sample with the CASI. AFM standards were used to show that focusing the CASI beam did not appreciably affect sample scatter as compared to a collimated beam (normal configuration). An optical microscope held in an adjustable stand was used to assist in centering the CASI laser on the patterned area. In-plane scatter was collected for un-patterned polystyrene and AFM-patterned polystyrene at 17 incident angles, ranging from 0° to 80°. Data was collected at two wavelengths: 544 nm and 633 nm. Both wavelengths showed strong negative first-order diffraction at high incident angles for patterned polystyrene. These orders were in excellent agreement with the classic diffraction equation for the known surface feature spacing. A single small resonant peak of unknown origin was also present at one incident angle for each wavelength.

## **II. Atomic Force Microscope (AFM)**

### **Overview**

This section provides a general understanding of the basic functioning of the AFM, outlines its most crucial components, and describes important experimental parameters. The intent of this chapter is to prepare the reader for the discussion of the AFM-patterned sample.

### **Basic Operation**

The AFM was designed to produce high-resolution images of both conducting and insulating surfaces. It operates by bringing a small tip, mounted on a cantilever beam, in close proximity to a sample surface. As the tip approaches and contacts the surface, forces develop that deflect the cantilever beam (Figure 1). As the tip is rastered back and forth across the sample surface, the deflection increases or decreases in response to the relative heights of surface features that the tip comes in contact with. This deflection is detected using a simple set-up whereby a laser is reflected off the top of the cantilever beam and into a quad photodetector [29]. A feedback loop adjusts the z-position of the tip and cantilever beam up and down with a piezotube (PZT) scanner to maintain a constant cantilever deflection. The amount of z-axis movement required to maintain a constant deflection at each point is stored and collectively forms an image of the sample surface.

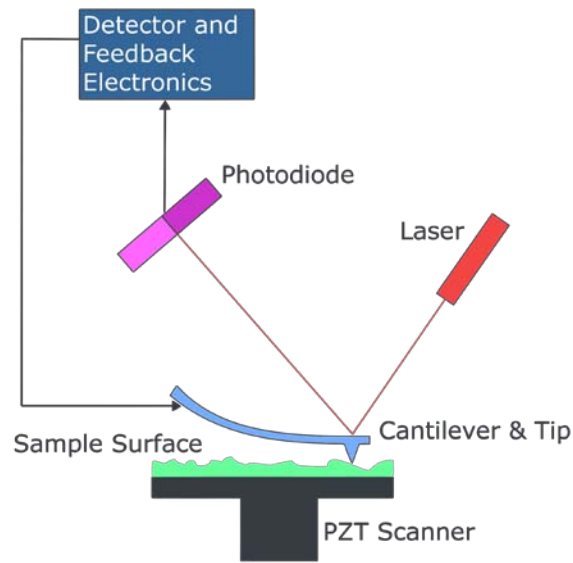


Figure 1: Atomic Force Microscope (AFM) diagram [30]

### AFM Instrumentation and Components

The AFM used in this work (Figure 2) was a Dimension V Scanning Probe Microscope (SPM) developed by Veeco Instruments. The complete AFM system also included a Nanoscope V controller and a computer workstation running the Nanoscope software, version 7.3.

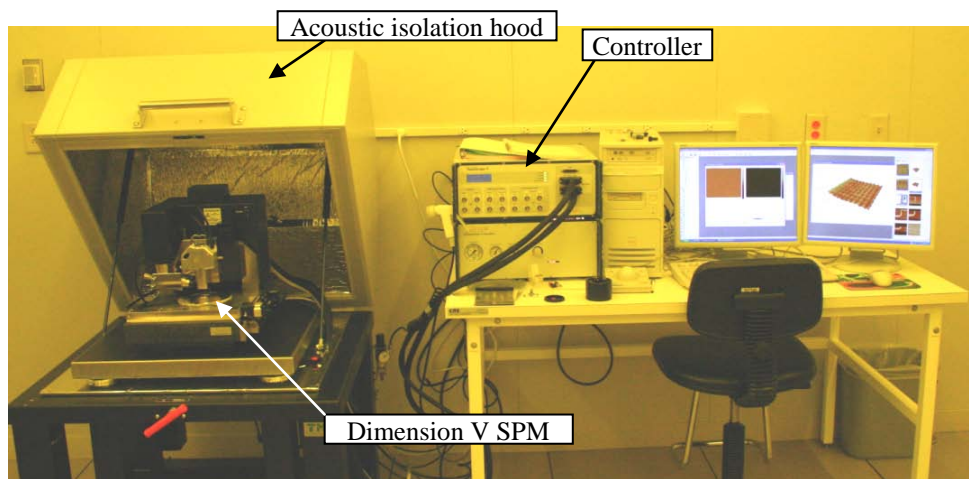


Figure 2: Dimension V SPM system.

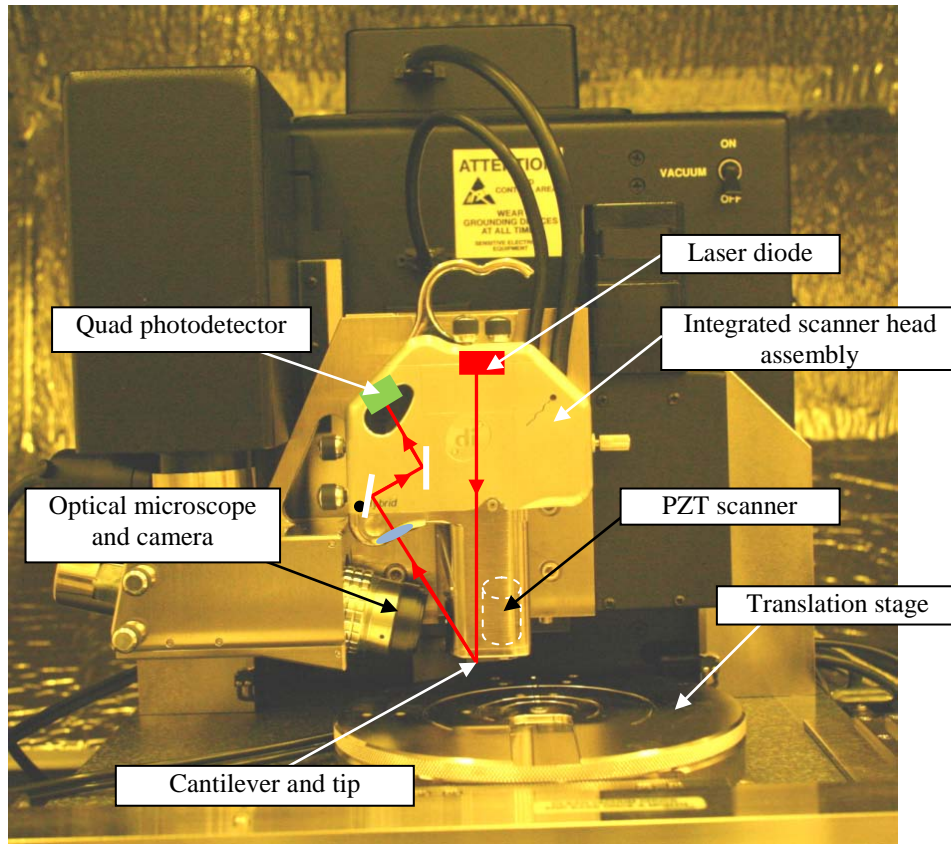


Figure 3: Dimension V SPM with schematic tracing laser path inside scanner head.

Like other AFMs, the Dimension V has two basic experimental components - the stage, which holds the sample, and the integrated scanner head, which holds the cantilever and tip. The stage on the Dimension V is circular, freely rotating, incorporates fully motorized X (range 120 mm) and Y (range 100 mm) movement, accommodates large samples, and is capable of micron-scale precision positioning [29]. The integrated scanner head assembly is mounted above the sample stage on a motorized Z-stage and combines both the piezoelectric tube scanner and the quad photodetector (Figure 3). The tip is mounted in a cantilever holder, which is inverted and mounted on pins on the bottom of the scanner head.

Assembling these components in this configuration offers two levels of relative tip-sample movement. Coarse positioning ( $\mu\text{m}$  to  $\text{mm}$  scales) is achieved through translation of the motorized stage (X and Y) and scanner mount (Z). During a translation, a puff of air lifts and lubricates the stage (it normally rests on a polished granite block) and two linear screw drives operate to move it in the X and Y directions. Once a location of interest is identified, the stage is locked in place and the fine movements (nm scale) of tip engagement and control (during imaging) are handled by the XYZ piezotube in the scanner head. Coarse movements are not made while the tip is engaged, as this could easily damage or break it.

In the context of this work, movements between individual pattern tiles are achieved by withdrawing the tip, moving the stage to position the tip at the center of the new tile, and then re-engaging the tip. Individual tiles are generated using the scanner exclusively, with the size of each tile limited by the scan range of the PZT ( $100\ \mu\text{m}$ ).

The Dimension V is an improvement over earlier AFM designs (those used in previous nano-patterning work). These instruments impose strict size limitations on sample size, requiring samples to be mounted on small metal pucks (1-2 cm diameter) that are magnetically mounted to an XYZ piezoelectric tube during imaging. In these designs, the cantilever is rigidly mounted above the sample surface and the sample is scanned beneath it. The scan range of the PZT on older AFMs is also smaller and coarse positioning is done using hand-adjusted screws. The design improvements incorporated into the Dimension V allow work of this type to be conducted.



Additional AFM components function to improve data quality and ease of operation. An optical microscope and camera is integrated into the Dimension V to aid in centering the tip over locations of interest on a given sample and in correctly setting the proper distance between the tip and surface before engaging the tip. An acoustic shield is provided to isolate the AFM from outside noise, increasing the image resolution.

Vibrations through the floor are reduced by the mass of the AFM's granite base and the soft polymer bumpers the base sits on. Critical also to the AFM system is the computer and software package that interfaces between the user and the instrument itself, relaying instructions from the user and interpreting the photodetector signals to generate an image.

### **AFM Software Operating Parameters**

Proper operation of the AFM depends as much on the operational parameters defined within the AFM's software as it does on the physical components. There are a multitude of parameters associated with the Dimension V. Happily, many of them are factory-defined and not normally adjusted by the user. There is, however, a significant number that are necessary to adjust during normal operation. These can be broken down into several categories – those needed for contact mode, tapping mode, ramping mode, and general operation. A basic understanding of these parameters is necessary for later discussion of patterning techniques.

Contact mode is the simplest AFM scanning mode and basic contact mode operation has already been discussed above. It is defined by the constant contact maintained between the tip and the sample. The amount of deflection that the AFM maintains is constant (maintained through feedback) and is specified by the value of the

deflection setpoint parameter, measured in mV. The deflection setpoint is directly correlated to force (through Hooke's law) – increasing the deflection setpoint voltage prompts the AFM to maintain a higher cantilever deflection and impart more force to the sample during scanning. Contact mode also generally uses a triangular cantilever to resist cantilever twisting.

Tapping mode (TM) is very similar to contact mode. Aside from using a straight cantilever, the most fundamental difference is that in tapping mode the AFM tip is oscillated up and down and lightly “taps” the surface, rather than remaining in constant contact. Tapping mode is especially important when imaging soft samples because for these materials “dragging” the tip across the surface can easily cause damage. In tapping mode, the tip is generally oscillated at its main resonant frequency by a separate piezoelectric stack in the cantilever holder (the cantilever holder used here accepted both contact mode and TM tips). The regular up and down motion of the AFM tip that results produces a sinusoidal photodetector signal [29]. A tip oscillation of large amplitude is started in free air, far from the sample surface. As the tip is then brought near to the sample surface, it begins to make contact at the lower oscillation extreme. The piezoelectric stack continues to input energy into the system at a constant rate, but this contact absorbs energy, dampens the oscillation, and decreases the oscillation amplitude. The decrease in amplitude is detected by the photodetector and the feedback loop adjusts the position of the z-piezo to return to a specified amplitude, defined by the amplitude setpoint parameter. The movement in the z-direction is used to construct the AFM image (as before). Decreasing the amplitude setpoint increases the force imparted to the surface

because the free air tip oscillation is dampened more strongly. Increasing the amplitude setpoint to values approaching the free air oscillation amplitude can cause the tip to lose contact with the surface. The amplitude setpoint is generally tuned to the highest value without losing contact between the tip and the surface. The proper resonant drive frequency is generally automatically determined using the included “Autotune” software function. Autotune also sets the oscillation drive amplitude to produce a pre-defined target amplitude. The target amplitude is the free air oscillation amplitude and is a good starting point for setting the amplitude setpoint [29].

Both contact and tapping mode make use of a feedback loop to maintain a constant deflection (contact mode) or amplitude setpoint (TM). The performance of this feedback loop is primarily dependent on two parameters – integral gain and proportional gain. Integral gain has the most pronounced effect, but both values determine the severity of the corrective response when the system deviates from the desired deflection or amplitude setpoint. Increasing the value of these parameters increases the size of the correction applied to the z-piezo. If the gains are set too low, the feedback response is not strong enough to keep the tip tracking the surface. This condition is most easily seen by comparing the trace and retrace. The trace is the scan line obtained in the forward direction; the retrace is the return scan line as the tip rasters back and forth across the sample surface. If the gains are too low, the trace and retrace will not align, especially near rapidly varying surface features. The gains should be increased only until the trace and retrace are aligned. Further increases will cause the feedback loop to overreact to surface perturbations and quickly overshoot the setpoint, setting up an oscillating cycle of

further over-corrections. This is an undesirable condition for general imaging (but is essential to induce ringing oscillations). While tuning the gains, it may be helpful to disable the slow scan axis. This prevents the AFM from advancing from the current scan line to the next one. Scanning the same line repeatedly enables the effect of an adjustment to be quickly determined.

Additional parameters are necessary for general AFM operation. Scan size defines the size of the AFM image produced and is limited by the range of the AFM piezotube. The absolute maximum scan size that the XYZ Hybrid Head used with the Dimension V is capable of is 100  $\mu\text{m}$ . However, the maximum size of the current scan is closely linked to and limited by the value of the X and Y offsets. The X and Y offsets define the center of the current scan. The absolute limits of the scanner are set once the tip engages the surface (Figure 4(a)). The offsets (dot in Figure 4) can be adjusted, but the new maximum scan size (Figure 4(b)) will be constrained by the original conditions present when the tip engaged. It should also be noted that the XY coordinate system from the user's point of view is opposite to that commonly used. That is, inputting a negative X or Y offset moves the offset in the positive X or Y direction or vice versa (as seen by the user on the screen). For example, the change in offset from Figure 4(a) to 4(b) is the result of a positive X offset and negative Y offset. This system is used later for moving the translation stage while moving from tile to tile as well.

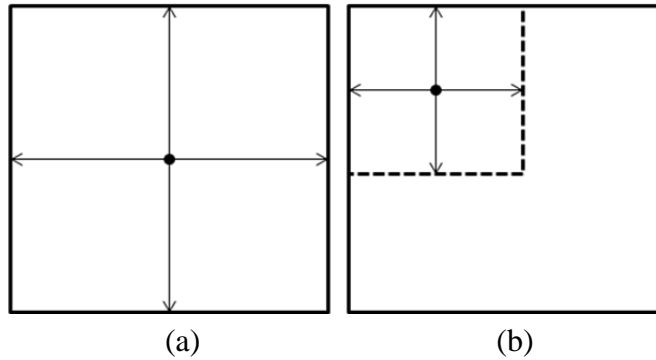


Figure 4: Relationship between scan size and X/Y offset

The shape of the current scan is controlled also by the aspect ratio, the ratio of side lengths (X/Y). Tip movement is primarily controlled by adjusting the scan angle and scan rate. The scan angle is the angle between the scan lines and the x-axis. The scan rate is defined in Hz – one cycle is a trace and retrace. The scan rate and scan size together define the tip velocity ( $\mu\text{m/s}$ ). High tip velocities increase the imaging rate but require higher gains to adequately track the sample surface and generally result in decreased image quality.

Image resolution is most heavily dependent on samples per line and number of lines. Generally, low values of these parameters are used for quick imaging to ascertain the general location of a surface feature of interest before increasing it to capture detail.

Many of the above mentioned parameters can be displayed either in volts or in metric units. Volts are a more fundamental unit, as the scanner movements result from voltages applied to the PZT. However, for practical reasons it is generally easier to work in metric distances.

The AFM is made possible because piezoelectric materials allow voltages to produce mechanical movement at the nanometer scale. However, the relationship

between voltage and movement is non-linear. The piezoelectric elements in an AFM scanner also suffer from hysteresis, a condition wherein it does not instantaneously return to its initial state when the voltage is removed. The exact nature of the non-linearity and hysteresis also changes as the piezoelectric crystals age. Together, this makes it very difficult to precisely predetermine the necessary voltage required for a desired piezoelectric response (movement). The AFM parameter called “XY closed loop” addresses this problem. When selected, this mode activates a closed feedback control loop on the XY piezo position that allows the AFM software to adjust the input voltage until the desired response is achieved. It is essential that the XY closed loop mode be enabled before operating in the AFM ramp mode.

### **Ramping Parameters**

The AFM ramping mode was essential to generating the patterned surface used in this work. Ramp mode is accessed from the tapping mode menu and uses tapping mode AFM tips; however, it does not involve tip oscillations, scanning the tip, or imaging the surface. Instead, the tip is simply lowered (as if to engage) until a predetermined deflection is reached and then the tip is retracted again. This imparts force to the surface and if the tip is stiff enough and the surface soft enough, an indentation will be left behind. Various ramping modes exist, but the ramping mode of interest for this work is “auto-ramp”. In this mode, the AFM automatically ramps at an array of specified locations. The user defines the center of the array (by setting the XY offset) and specifies the number of rows and columns. The distance between adjacent rows and columns is also specified.

In ramping mode, the tip is lowered to the sample through the application of a triangular potential to the z-piezo. The amplitude of this potential is defined by the ramp size parameter (mV or nm). The potential is applied relative to a position defined by the Z scan start parameter. Increasing Z scan start moves the starting point for the cantilever closer to the sample. If the ramp size is greater than the starting distance between the cantilever and the surface, at some point during the ramp, the tip will make contact and the cantilever will deflect.

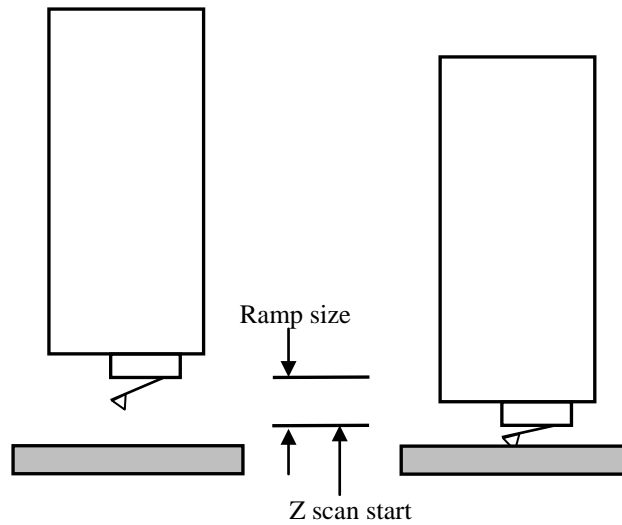


Figure 5: Illustration of ramp size and Z scan start

The response of the AFM to this deflection (in auto-ramp mode) is governed by the trigger mode. If the trigger mode is disabled, the entire potential (ramp size) will be applied regardless of when (or if) contact is made. If trigger mode is enabled, there are two options: absolute and relative trigger mode. Both are designed to limit the amount of force imparted to the sample by the descending tip by “triggering” the AFM to prematurely stop applying the triangular potential and lift the tip at a defined point. In absolute trigger mode, this point is specified by a deflection setpoint value and set

relative to a constant arbitrary point. Alternatively, relative trigger mode uses an additional parameter (trig threshold) to specify the amount of additional deflection to be allowed, relative to the un-deflected cantilever beam. Relative trigger mode offers the benefit of operating independently of the mechanical and thermal drift that typically occurs during long AFM running times [31] and was the trigger mode used in this work.

In auto-ramp mode, the AFM moves through the pre-programmed array, performing one ramp cycle at each location. The speed at which it does this is governed by the scan rate. In turn, scan rate is dependent on forward and reverse velocity, the speed with which the tip is lowered and retracted during the ramp cycle. The ramp size also factors in to scan rate. Faster velocities and smaller ramp size translates into a faster scan rate, a consideration that becomes more important as the size of the array being generated grows.

As indicated in previous figures, the AFM cantilever is mounted in the cantilever holder at a slight downward angle. Because of this, when the tip is lowered in the z direction during ramping, it has a tendency to move laterally and plow the surface (usually in the x direction) during indentation. To compensate for this, a small movement can be added to the x direction during ramping. The parameter controlling the compensation is called X rotate (deg).

## **Summary**

This chapter outlined the basic functioning of the Dimension V AFM, including its most crucial components and important experimental parameters, in preparation for the following discussion of the production of the AFM-patterned sample.



### **III. Sample Production**

#### **Chapter Overview**

Three different techniques were investigated to produce a periodic array of surface features on a polystyrene film on a silicon substrate. Two of them involved scanning while inducing tip oscillations to turn the tip into a nano-hammer. The first used a Force Modulation (FM) AFM tip holder to induce the oscillations; the other induced them using a “ringing” feedback condition. The third made use of an existing auto-ramp mode present as an optional Dimension V capability. The oscillating tip techniques were unsuccessful, due largely to small tip oscillation amplitudes and inappropriate oscillation frequencies (for this application) generated by the Dimension V. The nano-indentation technique, together with a “floor-tile” patterning approach, yielded a patterned sample 325  $\mu\text{m}$  by 200  $\mu\text{m}$  in size. The distance between surface features was 400 nm and their relative height was 140 nm.

#### **Substrate Preparation**

The polystyrene film used in this work was prepared from a 2.0% polystyrene in toluene solution. It was originally prepared for use in previous nano-patterning work conducted by Li and Burggraf at the Air Force Institute of Technology (AFIT) [24-25]. The polystyrene was coated on single-crystal Si wafers using an accelerating flow-coating process, previously reported by Juhl *et al.* [32]. The molecular weight of the polystyrene was 233 kg/mole. The polystyrene thickness was mapped by conventional ellipsometry imaging and found to have a uniform thickness gradient ranging from 20 to

240 nm. The thickness of the region patterned in this work was found to be approximately 120 nm through AFM imaging of a nearby thickness scratch (Figure 6).

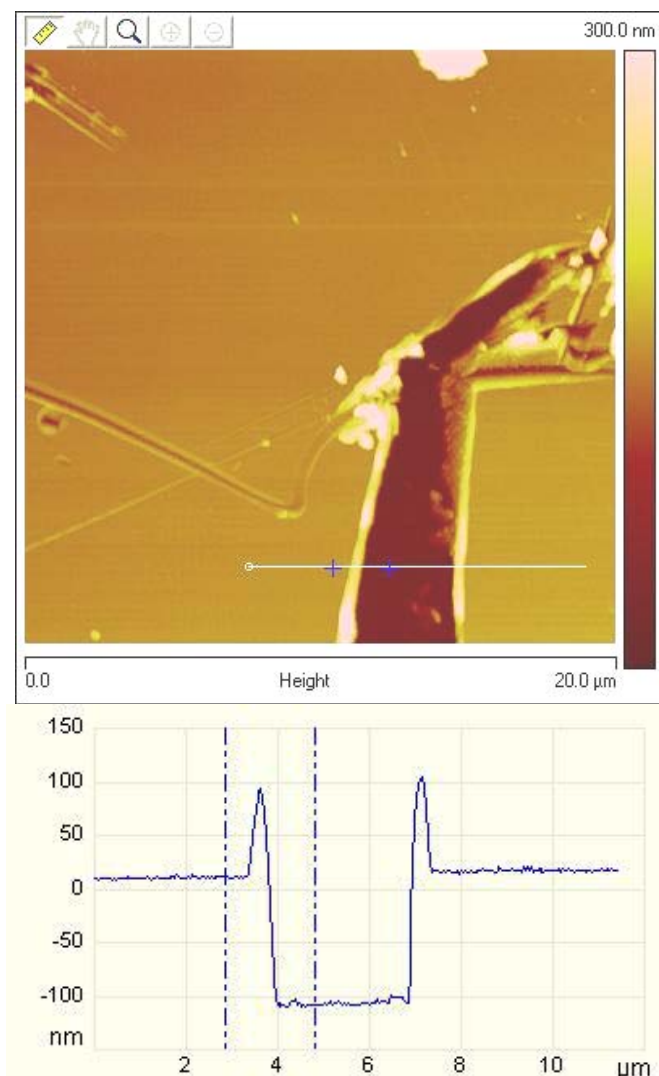


Figure 6: AFM image of the surface scratch, including cross section showing its depth (120 nm)

The previous work conducted by Li and Burggraf only consumed a fraction of the polystyrene samples prepared; the remainder was covered and stored in a low-humidity environment for approximately 3 years. This kept the surface clean and large areas of the polystyrene surface were free of visible outside contaminants. The polystyrene surface

was also exceptionally flat prior to this work. The cleanliness of the polystyrene surface was maintained during pattern generation by working in a clean room environment (class 1000).

The polystyrene was originally deposited in two blocks near the center of a round silicon wafer (approximately 4 inches in diameter). The strip of silicon containing the polystyrene blocks was later scored along a straight edge and removed.

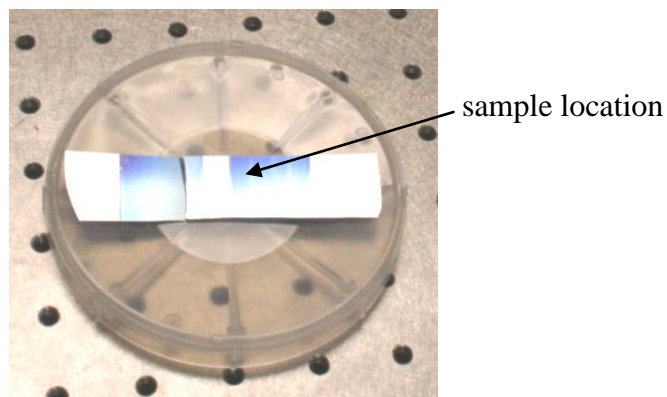


Figure 7: Polystyrene film on silicon substrate, arrow showing approximate location of patterned area

### **Force Modulation (FM)**

Force modulation (FM) is a hybrid of contact mode and tapping mode and uses a specialized cantilever holder. In FM, the tip is scanned at a constant deflection as in contact mode. It is also oscillated at the resonant frequency of a large piezoelectric bimorph in the cantilever holder. FM was conceived as a way to distinguish between different materials in a composite because soft materials allow the tip to penetrate more deeply (and produce smaller deflection) than hard materials.

It was originally thought that FM may allow for a high degree of control over the surface feature period. While oscillating at a constant resonant frequency, adjusting the

scan speed (by adjusting the scan rate and scan size) would allow precise wavelength (period) control ( $v = f\lambda$ ). The relative softness of polystyrene and the large size of the FM piezoelectric stack (able to produce strong oscillations) also made FM a promising technique [29].

However, the resonant bimorph frequency of the FM cantilever holder is rather high (9.3 kHz), requiring the AFM tip to be scanned at high tip speeds to space out the nano-hammer “strikes” to the desired feature spacing (120 nm). High tip speeds are desirable in the sense that they would allow patterns to be generated quickly. However, at high tip speeds, the AFM cannot properly track the surface. Increasing the gains to compensate causes tip instability and oscillation. The strength of the bimorph resonance is also much smaller than the cantilever resonance used in tapping mode, requiring the large driving amplitude capability of the FM bimorph to generate the small oscillations necessary for FM imaging (but too small for modification). For these reasons, efforts to generate nano-patterns with FM as originally planned were unsuccessful.

It was previously noted that increasing the gains at high scan speeds while operating the FM tip produced tip oscillations. Experimentation allowed periodic ringing oscillations to be achieved. Figure 8(a) shows the path of the oscillating FM tip. The oscillations were strongest at the beginning of a scan, dampening out towards the end. However, the trace (blue) and retrace (red) reinforced each other, allowing a pattern of ridges to be produced (Figure 8(b)). Unfortunately, because the amplitude of the oscillations was very small (about 3 nm), the ridges were very faint, too small for surface reconstruction (Figure 8(b)).

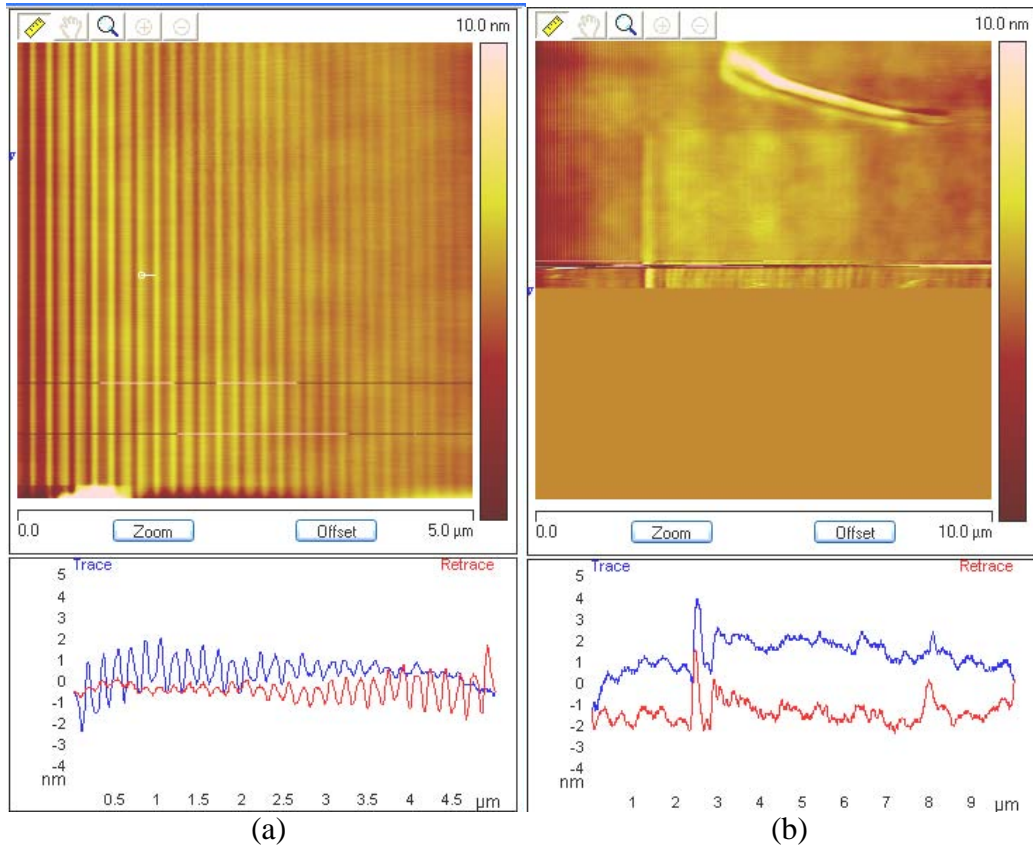


Figure 8: (a) FM ringing patterning (b) faint ringing FM patterns

### Ringling Oscillations

As previously mentioned, successful AFM patterning of polymer films was previously demonstrated on smaller, bench-top AFM designs using a ringing feedback control condition [24-25]. In this technique, the integral and proportional gains, normally tuned to track the surface, are greatly increased. This produces a feedback condition where the instrument overreacts to small system perturbations and wildly overcorrects. This overcorrection, when detected, induces another AFM correction in the opposite direction. Because the integral and proportional gains are set so high, this correction is also too strong. The resulting condition produces standing waves across the AFM scan

(Figure 9(a)). These standing waves are critical to the success of this technique because they ensure that as the AFM tip scans across the same scan area (10-25 times) the points of impact of the AFM tip are in phase and reinforce one another. Over time, these impacts create a set of ridges, perpendicular to the scan direction. Shifting the scan direction by  $90^\circ$  and repeating the procedure will produce a second perpendicular set of ridges. The superposition of the two sets of ridges produces an array of nano-dots [24-25].

Initial attempts to achieve a similar ringing condition on the Dimension V were unsuccessful, prompting the pursuit of FM as an alternative method. The discovery of a ringing feedback condition while using FM stimulated further ringing oscillation experimentation.

The primary reason that initial efforts failed to produce ringing oscillations was that a discrepancy existed between the respective gain scales of the Dimension V and the AFM model used in previous work [24-25]. Ringing oscillations were produced in previous nano-patterning work at gain settings of 2-3 and fractional changes produced a large effect. This experience was applied to the Dimension V and when gains of 10-20 failed to produce ringing oscillations, the conclusion was made that the underlying instrumental instability exploited in previous work had been corrected in the design of the Dimension V. Probing the instrumental limits of the Dimension V while working with the FM cantilever holder showed that oscillations could be produced, though the integral and proportional gains needed to be set to 40 and 70 respectively, levels previously thought to be impractical for AFM operation (much higher than previous work).

Using this experience, a standard AFM cantilever holder operated in contact mode with a triangular cantilever allowed higher quality oscillations to be excited and a series of patterned ridges to be produced (Figure 9). However, these patterning efforts were inadequate in several respects. First, the oscillation amplitude was still very weak, being a very modest improvement over FM results. This required 30 minutes of scanning to produce small (10 nm high) surface ridges. There was also inconsistency in feature height across a given pattern resulting from the damping of the oscillations (Figure 9(b)). Equivalent ringing oscillations were not achieved under a 90° scan, a crucial capability for generating two-dimensional patterns. Lastly, the number of oscillations in a scan was largely dependent on scan rate and gain settings, not scan size. This meant that for small scan sizes (5-10  $\mu\text{m}$ ) the feature spacing was small (100-200 nm). However, as the scan size was increased, the number of oscillations remained constant and were merely spaced further apart, increasing the feature separation in proportion to the increase in scan size. This limitation would require either a relaxation in desired feature spacing or the generation of many times as many tiles, both options being untenable.

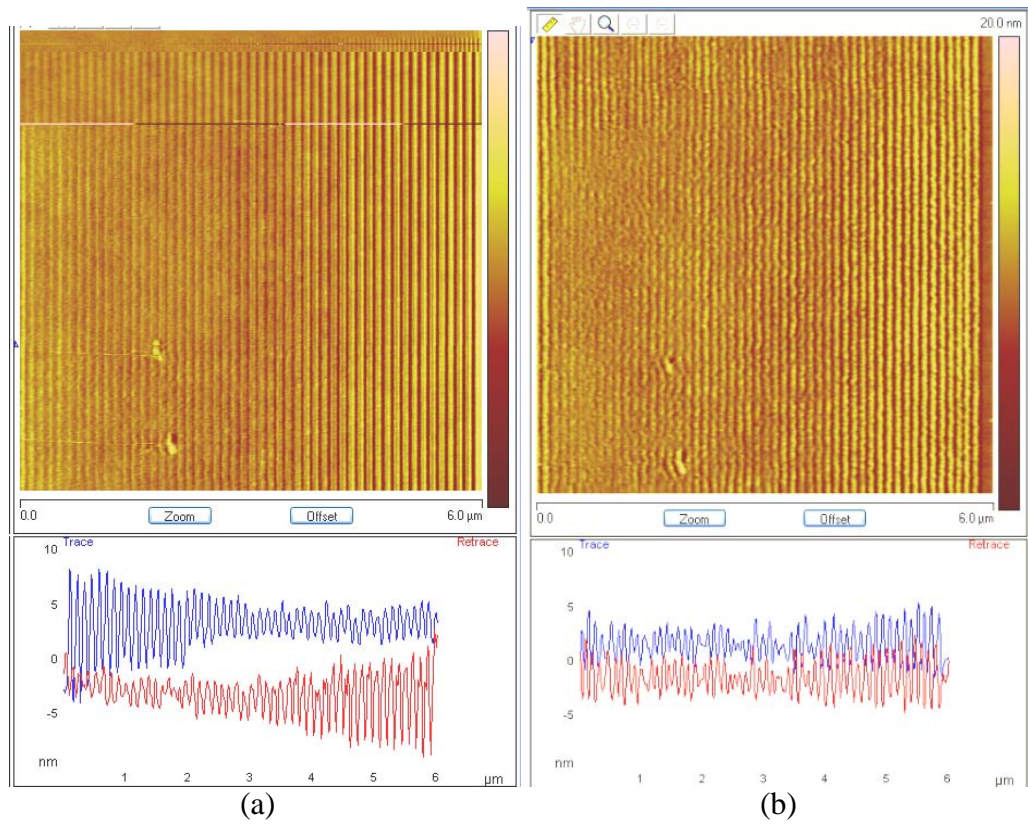


Figure 9: (a) Patterning with ringing oscillations and (b) image of resulting pattern

Efforts to produce patterns as originally planned were further hampered by the realization that the ability to automatically program the AFM to move to a series of predetermined positions and image according to preset parameters was limited to locations within the current scan range only. This was inadequate for the purposes of this work as the objective was to create tiles requiring the entire scan range. Creating many adjacent tiles would therefore require extensive user manipulation to withdraw the tip, translate the stage, and re-engage the tip between the patterning of each tile.



### Nano-indentation with Diamond AFM Tip

The third technique investigated was nano-indentation with a diamond AFM tip. This technique produced a successful pattern, 325  $\mu\text{m}$  wide by 200  $\mu\text{m}$  tall. The feature spacing was 400 nm and their relative (peak-to-valley) heights were 140 nm. A magnified image of the completed pattern is shown in Figure 10. This image was taken with the AFM optical microscope used for sample positioning. The shadows in the image are from the AFM tip, located directly above the patterned area. A high-resolution AFM image of the pattern surface is shown in Figure 11.



Figure 10: Completed AFM-patterned 2-D thin-film photonic crystal (each pattern is numbered in lower left corner in the order they were produced)

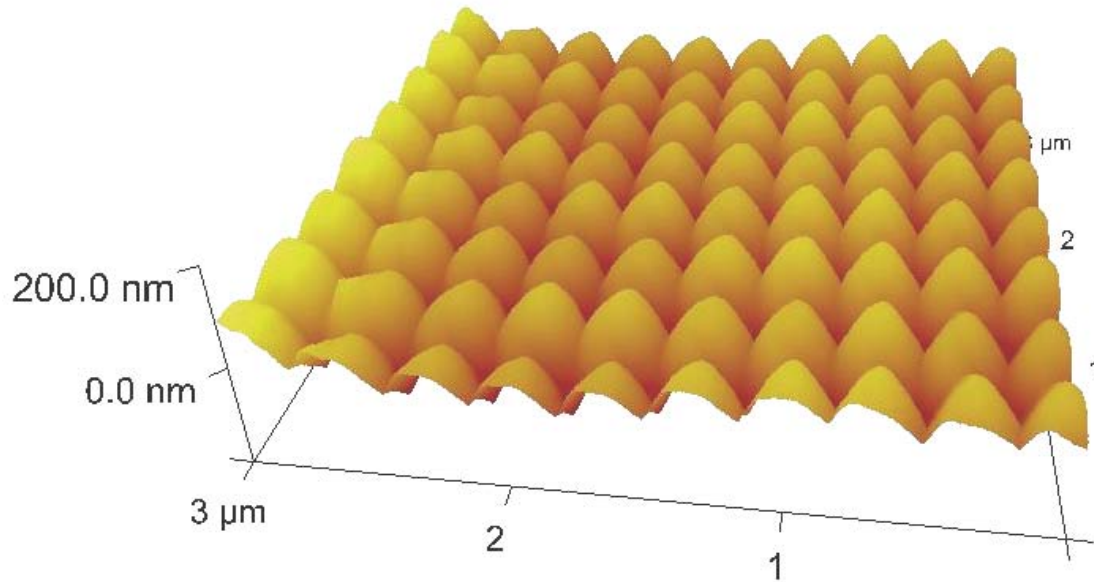


Figure 11: AFM image of the patterned surface

The basic operation of the AFM ramping mode was covered as part of the discussion of general AFM operation in Chapter II. AFM nano-indentation is performed using the native auto-ramping functionality already present on the Dimension V. The primary additional component for nano-indentation is a specialized indentation probe.

Indentation probes have straight cantilever beams (like standard TM cantilevers) but are much thicker, wider, longer and are made of stainless steel instead of silicon or silicon nitride. The spring constants of indentation probes are also much higher (100-300 N/m) than either TM probes (20-100 N/m) or contact mode probes (0.01-1.0 N/m) [31]. The spring constant of the indentation probe used in this work was 186 N/m. The diamond tip was produced through precision grinding of a solid diamond and is designed to be strong enough for repeated nano-indenting applications [33]. The tip point has a nominal radius (when new) of 40 nm and is shaped like the corner of a cube (the

intersection of three right angle planes). To assist in producing symmetric indentations, the tip is mounted with its vertical axis approximately normal to the sample when secured in the cantilever holder and mounted in the AFM (though X-rotate of  $12^\circ$  was still required). The nano-indentation tip used here was the DNISP, made by Veeco Instruments [33].

Even though a nano-indentation probe is much stiffer than a normal TM probe and designed for the indentation of materials, it is still capable of limited traditional TM imaging. However, the resonant frequency of an indentation probe (35-60 kHz) is generally much lower than TM probes (300 kHz). This capability is especially valuable for this work because it allows an indentation (or completed indentation array) to be immediately imaged after generation for verification purposes.

As previously mentioned, the Dimension V offers a developed capability to carefully control the amount of force imparted to the surface during a ramp cycle using the relative trigger mode and setting a trigger threshold. Efforts were made to impart a uniform force between tiles by maintaining consistent trigger threshold values. However, in this instance, it turned out to not be strictly necessary. Because the polystyrene film was so soft, it offered very little resistance to the stiff cantilever and hard diamond tip. Thus, whenever contact was made during the ramp cycle, the tip plunged to the bottom of the film. It was prevented from penetrating further by the much harder silicon substrate. This situation provided a measure of inherent feature consistency, very tolerant of differing trigger threshold settings. The indentation consistency throughout an array is shown in Figure 12.

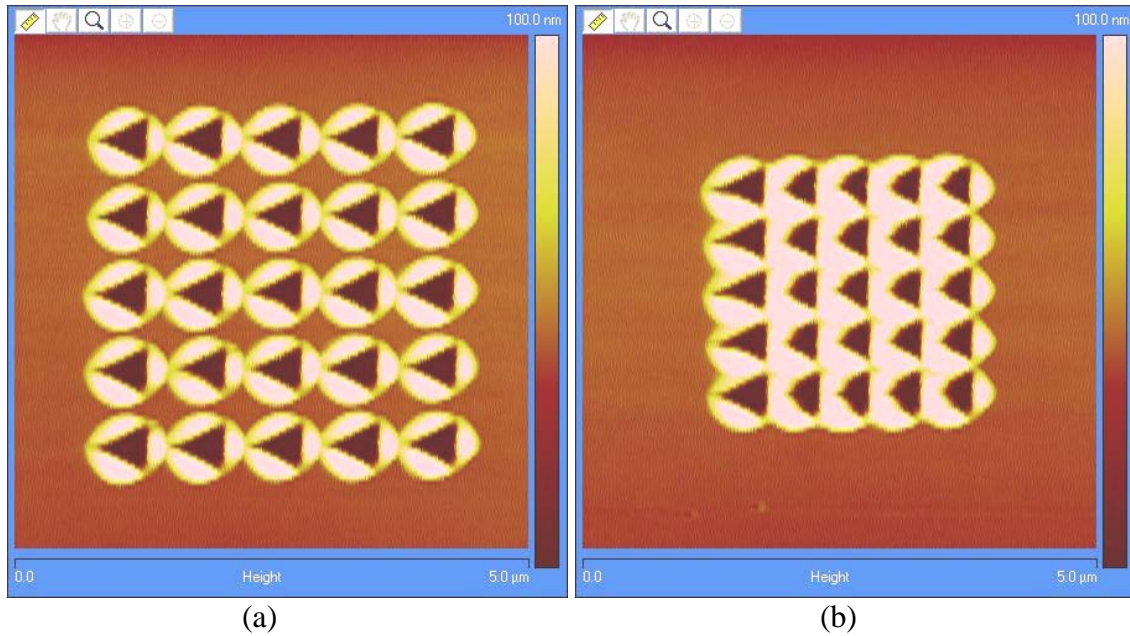


Figure 12: 5 x 5 Nano-indentation trial arrays showing indentation consistency and the effect of feature spacing.

(a) 750 nm spacing (b) 500 nm spacing

Figure 12 also shows the affect of indentation spacing as well as the mounding up of displaced material at the indentation edges. At 750-nm spacing (Figure 12(a)), the edges of adjacent indentations begin to touch. Decreasing spacing to 500 nm causes them to overlap and the interior features begin to assume a uniform shape (Figure 12(b)). The effect is even more pronounced at an indentation spacing of 400 nm (Figure 13). Here, the features are particularly easy to see. 400-nm spacing was near the limit for this combination of tip shape and film thickness. Decreasing the spacing any further would have overlaped the indentations, decreasing feature quality and increasing patterning time per tile.

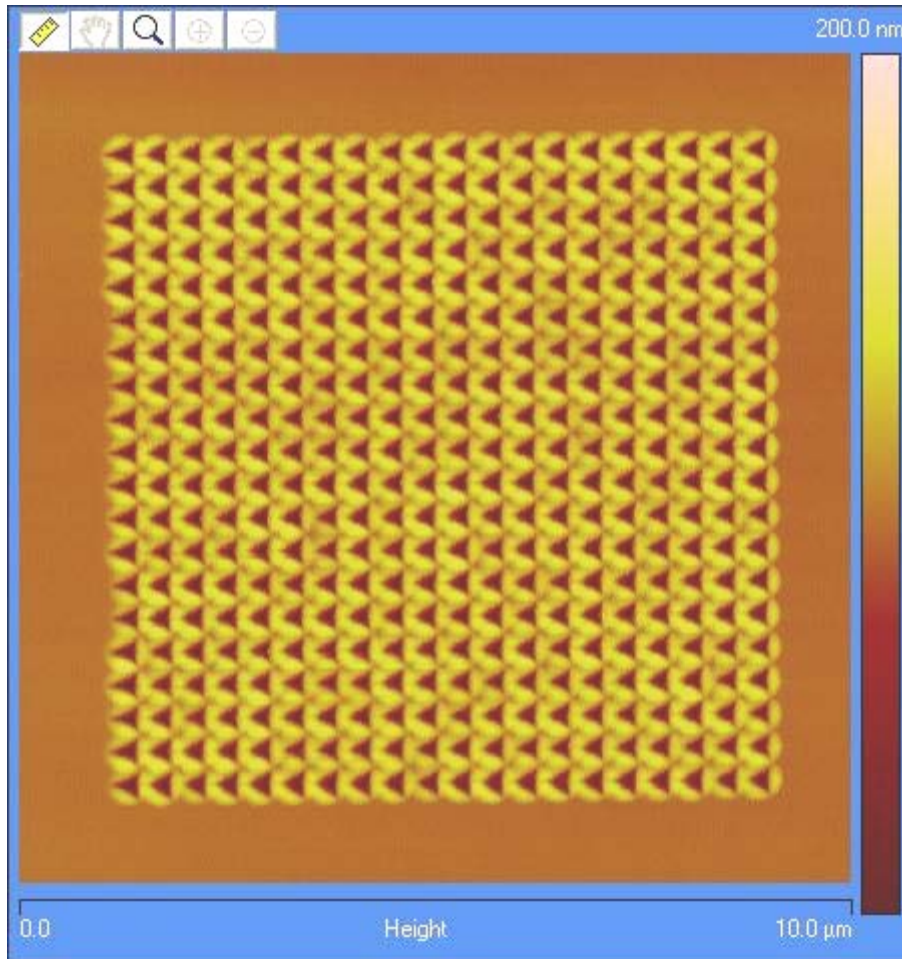


Figure 13: 20 x 20 nano-indentation array, 400 nm spacing

The auto-ramp function within the Dimension V software makes generating a single array a simple matter of inputting the number of rows and columns and specifying the feature spacing, then hitting go. From this point (as long as the XY closed loop is enabled), the AFM proceeds automatically and will generate a high quality tile, limited in size by the scanner range. As originally equipped, the XYZ Hybrid scanner head in use with the Dimension V has a maximum XY range of approximately 100 μm (-50 μm to +50 μm). However, while increasing the size of an individual tile, it was discovered that the scanner had previously sustained some damage to the Y piezo that limited its

maximum movement in the  $-Y$  direction (up) to half of its full extension (approximately  $25\text{ }\mu\text{m}$ ). The effect of this is clearly seen near the top of Figure 14 where the same scan line is repeated. In this instance, a signal is being sent to the scanner to move to a particular position but the piezoelectric crystal is unable to respond, so the scan line at its limit is simply repeated. This limited the maximum size of a single square patterned tile to  $50\text{ }\mu\text{m}$  on each side. This equates to a  $125 \times 125$  2-D array. The first five tiles in the first row of the completed pattern were  $50\text{-}\mu\text{m}$  tiles.

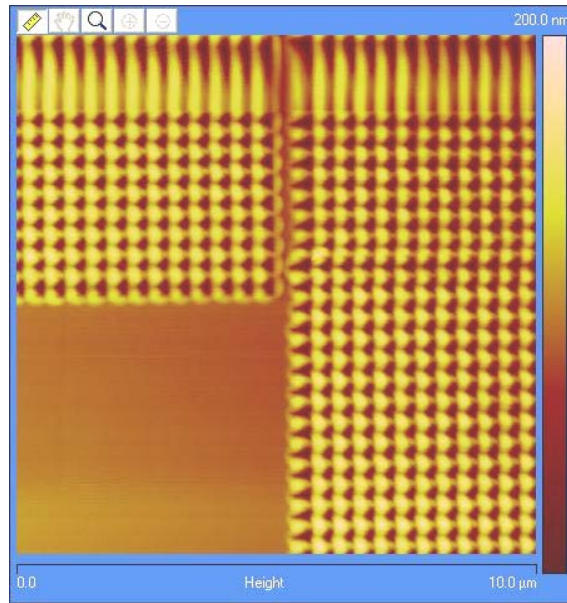


Figure 14: Example of reduced Y scanner range.

It was found through the course of this work that the tile sizes could be increased by relaxing certain restrictions. Because the scanner was undamaged in the X direction, the tiles could be extended in X, creating rectangular tiles. This was done for the tiles in the second, third and fourth rows, decreasing the number of tiles from six to four. Because the Y scanner was undamaged in the  $+Y$  direction (down), the Y dimension of the tiles could be slightly extended by shifting the offset in the positive direction. These

two considerations allowed the size of an individual tile to be increased from 50 x 50  $\mu\text{m}$  to 80 x 60  $\mu\text{m}$ .

While operating near the edge of the scanner range in auto-ramp mode to generate large tiles, it is important as well to set the scanner to a small scan size (1  $\mu\text{m}$ ) immediately before switching to ramp mode. An inverse relationship exists between scan size in scan mode and the maximum scanner range in ramp mode.

Once suitable operational ramp parameters have been determined, generating individual tiles requires little monitoring. The difficult part of the process is translating from the current tile to the proper position to generate the next one. Because the precision of the scanner is much higher than the translation stage, it is desirable to generate the largest tiles possible and operate near the scanner limits, patterning the largest area with the fewest number of tiles. This imposes strict limitations on where the offset can be to reach the extremes of the scanner's range (see Figure 4 in Chapter II). Furthermore, this precise offset position must be achieved using the translation stage, an operation made more difficult by the coarse nature of the translation stage movements.

The uncertainty in the translation stage can make positioning the tip properly largely trial-and-error, requiring multiple tip withdraw-movement-re-engagement cycles to achieve proper tip placement. However, the uncertainty in stage movements can be reduced by consideration of the backlash of the motorized linear drive screws. Backlash refers to the small amount of extra space present between the two sets of interlocking screw threads in the drive screws. In any translation, the screws must take up this small gap before they will actually move the stage. Thus, backlash can be mitigated by

translating repeatedly in the same direction. To this end, it is helpful to make a few translations in the same direction before starting the first pattern and then to pattern in a zig-zag motion down the rows of the tiled array. In this manner, backlash will be a factor only at the turn-around at the end of the rows.

The procedure used for tiling multiple patterns together involves several steps. When the current tile completes its auto-ramp sequence (4-8 hours, depending on size) the AFM will wait for further instruction. At this point, switching back to scan mode (TM) allows the surface to be imaged to ensure the indentations were created properly. Manipulate the offsets and scan size to run a small scan at each of the pattern corners to assess the quality of the inter-pattern interfaces. If the patterned tile was indented properly, withdraw the tip. The AFM will return to a (0, 0) offset before withdrawing, leaving the current tip position at the center of the current pattern. If the pattern quality is poor (or the AFM failed to pattern), the soft polystyrene surface can be re-patterned before the tip is withdrawn.

Input a stage translation that is slightly smaller than the desired spacing between adjacent tile centers to ensure that the scanner will be able to extend back to the edge of the tile just completed, keeping in mind that the coordinate system is reversed and also considering backlash.

Care must be exercised before engaging the tip to avoid damaging the polystyrene surface. Before engaging (especially for the first time), it is important to run the “locate tip” routine (from the navigate window) and bring the tip into sharp focus. This allows the AFM to exactly determine the Z-position of the tip. Then the sample surface is



normally brought into sharp focus. In this configuration, the AFM tip and the sample surface are a preset distance apart (usually 1 mm). When the tip is engaged from this configuration, the AFM quickly lowers the tip to within 100  $\mu\text{m}$  of the surface using the motorized Z stage and then slowly extends the Z piezo until contact is made and a deflection is detected. As the tip is extended further and further, the AFM continuously reduces the rate of extension to allow for contact to be made softly.

Engaging from a sharply focused surface is appropriate for hard samples. For polystyrene, it was found that this sequence did not always engage softly enough to avoid damage. Some of the resulting dimples can be seen in the image of the completed array at the center of several individual tiles (Figure 10). These center dimples could be avoided by engaging from a slightly further point. This was done by finding the sharp surface focus and then de-focusing outward slightly. This caused contact to be made at a point in the engagement process where the tip was extending more softly.

Properly engaging the tip was also important because it affected the speed of the later auto-ramp sequence. A hard tip engagement typically translated to slower auto-ramp cycles.

Once engaged, adjust the offsets and scan size to image a corner of an adjacent pattern. From this image, offset on a corner indentation of this pattern. To these X and Y offset values, add or subtract the appropriate integral number of feature spacings to move the offset to the center location of the new pattern. Account for the space between the two patterns and pattern odd numbers of rows and columns so that an indentation will be located at the exact center of the new pattern (an even number of rows or columns will

cause the pattern to be shifted by  $\lambda/2$ ). This new offset location will be the center of the new pattern – ensure that the known scanner range is enough to reach all edges of the new pattern. If it is not, it is likely due to error in the stage translation. This can only be corrected by withdrawing the tip, making a small translation (include backlash) and re-engaging.

Precise tip engagement and offset calculation help to ensure that the new pattern is correctly positioned. However, the thermal and mechanical drift of the AFM can impart slight deviations. Thermal drift can be mitigated by patterning with the acoustic isolation hood open to maintain thermal equilibrium (electronics generate a lot of heat). This benefit is more important for this application than preventing fine acoustic disturbances. Mechanical drift occurs as the AFM scans for a long period of time. To mitigate mechanical drift, it is important to start the auto-ramp sequence as soon as possible after setting the final offset.

Another potential source of surface damage can occur as a result of the initial value of the Z scan start. Z scan start is the furthest point that the Z piezo extends during a ramping cycle. When entering ramp mode from TM mode, it is initially set as the previous average Z piezo position [29]. This average position is dependent on the surface topography being imaged just prior to entering image mode. If un-patterned polystyrene was being imaged, then the average Z-piezo position is likely to be above the polystyrene surface. However, if the previous pattern was being imaged instead, with its peaks and valleys, the average Z-piezo position would likely correspond to a position below the level of the un-patterned polystyrene (Figure 15).

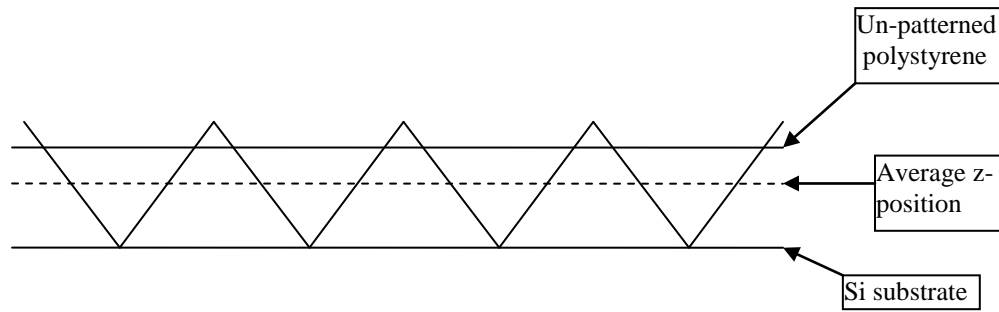


Figure 15: Automatic initial Z scan start value when entering ramp mode.

When the auto-ramp sequence is initiated, the tip lowers to a position corresponding to the Z scan start position plus the ramp size and then moves to the position of the first indentation. If an automatic Z scan start position that is too low (after adding the ramp size) is not corrected, this movement will scratch the surface across the tile diagonal. To guard against this damage, it is important to make sure that the Z scan start is always negative (above surface level) before starting an auto-ramp routine. Relative to this, the exact magnitude of Z scan start is unimportant as long as it is low enough for the tip to make contact and satisfy the trig threshold before exhausting the ramp size.

Ramp size can be very large without affecting the patterning results. Large ramp sizes merely force the AFM to start each ramp at a further retracted position. It does, however, negatively affect the speed of patterning as large ramp sizes take longer to execute and additional retraction after the tip breaks contact is unnecessary. It was generally satisfactory to operate with a Z scan start of -200 nm and a ramp size of 600 nm. Increasing forward (extension) and reverse (retraction) tip velocities increased the patterning speed, but only to a point (increasing beyond 10  $\mu\text{m/s}$  had little additional benefit).

It is important to maintain the patterning conditions as consistently as possible from run to run. If possible, leave the tip and sample undisturbed. If the sample must be removed from the AFM, document (and mark) the position of the sample so that it can be returned to as close to the same position as possible. If the tip must be removed from the scanner, make every attempt to avoid removing the tip and cantilever from the cantilever holder. The holder is aligned on the scanner with pins, but the cantilever is positioned in the holder by hand and is almost impossible to reposition exactly. It is also recommended that the edge of the AFM pattern be generated to be parallel with a macroscopic edge of the sample material. This assists greatly in later CASI alignment.

The considerations mentioned here are general guidelines from experience gained in this work. However, a considerable amount of experimentation is typically necessary to optimize any AFM process. Patterning mistakes and imperfections can be corrected using the offset techniques described above. Small patterns can be generated to fill in gaps and the soft polystyrene surface can be re-patterned if necessary.

## **Summary**

Three different techniques were investigated to produce a periodic array of surface features on a polystyrene film on a silicon substrate. Two of them (Force Modulation and ringing oscillations) were unsuccessful. The third, auto-ramped nano-indenting with an AFM diamond tip, yielded a patterned sample 325  $\mu\text{m}$  by 200  $\mu\text{m}$  in size. The distance between surface features was 400 nm and their relative height was 140 nm. Important considerations and guidelines when performing nano-indentation on polystyrene are also covered.

## **IV. Complete Angle Scatter Instrument (CASI)**

### **Chapter Overview**

The purpose of this chapter is to serve as a brief introduction to the layout and components of the CASI system and to describe additional procedures necessary to collect BRDF data for very small samples.

### **Complete Angle Scatter Instrument (CASI) System**

The CASI system was designed as a nondestructive way to evaluate surface quality on a variety of materials. To do this, CASI directs laser light (544 nm, 633 nm, 3.39  $\mu\text{m}$ , or 10.6  $\mu\text{m}$ ) from a source box onto a sample mounted on a stage. Light transmitted and reflected from the sample surface in the plane of incidence is collected by an aperture and measured by a single element photodetector mounted on an arm that sweeps out a full arc around the sample [34]. These measurements, along with the aperture size, distance to the sample, and initial incident power on the sample, are then used by the computer to calculate a BSDF (Bi-directional Scatter Distribution Function) [4].

The complete system has two source boxes, each housing two laser wavelengths (one visible and one IR). Each source box (Figure 16) contains several components that split, focus the beam, and direct it onto the sample. The beam is split to allow a chopper to modulate the beam for optical lock-in detection (to filter out noise) and for a wide band detector, which helps cancel out laser instability. A turning mirror is used to direct the laser beam through an objective and pinhole mounted on a moveable track (together

referred to as the focus stage). This allows the focus of the beam to be adjusted. After the pinhole, the laser is directed to an off-axis parabolic mirror which reflects the beam toward the sample [35]. To polarize out-going light, a half-wave plate and linear polarizer is inserted in the beam path prior to the objective.

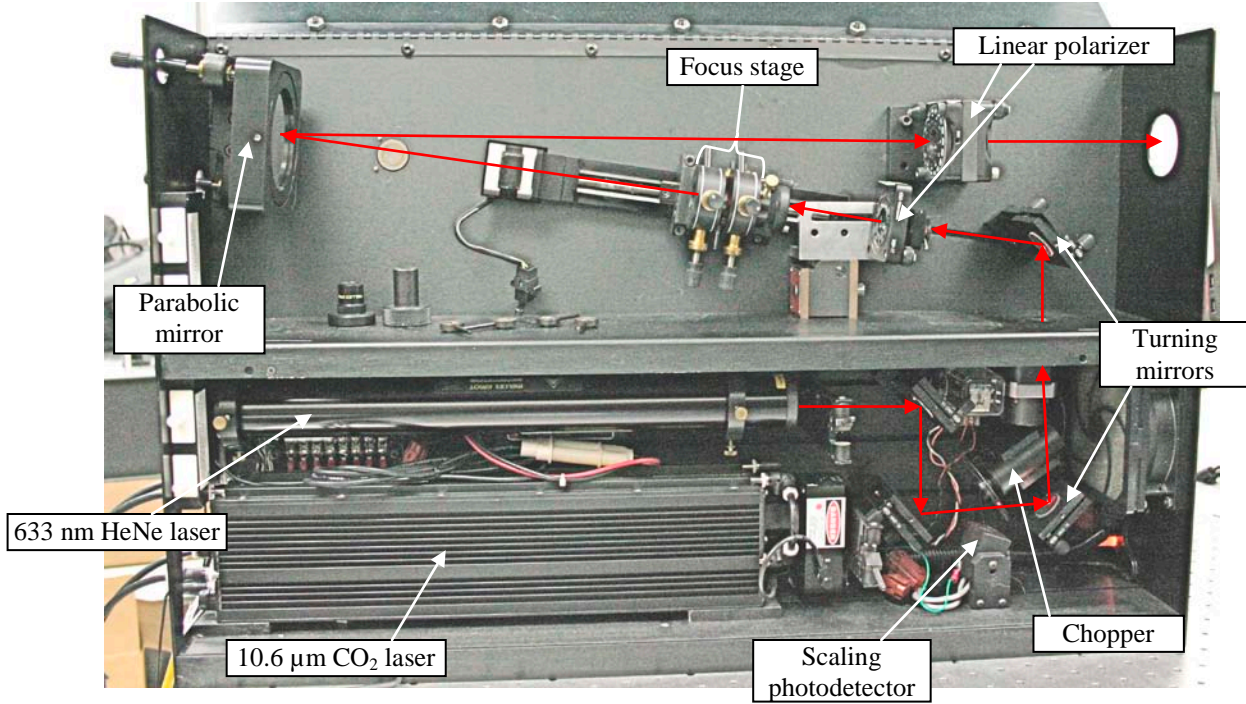


Figure 16: CASI source box [4].

The sample is mounted on the CASI's rotation stage (Figure 17), which is capable of translating the sample in X, Y, and Z as well as two-axis tilt and rotation. In this work, all samples were mounted on metal pucks with double-sided tape and magnetically mounted in the CASI.

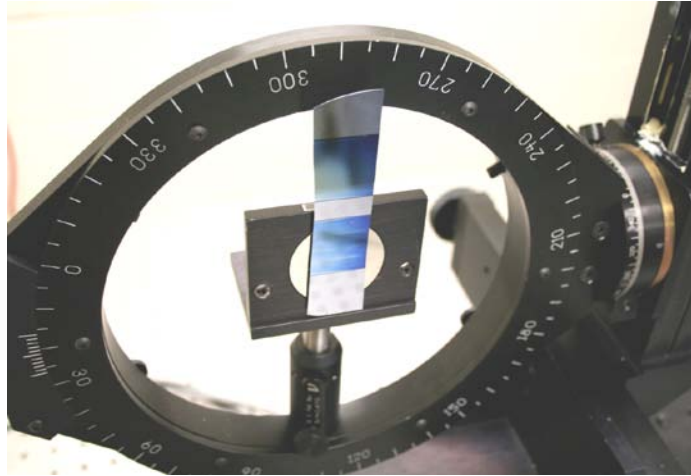


Figure 17: Sample mount (AFM-patterned sample)

### **Normal CASI Operation**

Normal CASI alignment procedures are straight forward and previously documented by Mr. Dominic Maga [36]. Reproducibility of CASI measurements is highly dependent on careful and consistent alignment and benefits greatly from experienced operators. CASI data used in this work was gathered by Mr. Maga, a laboratory technician with extensive CASI experience.

In normal CASI operation, the focus stage is positioned to focus the laser beam at the detector with the beam passing directly through the sample. This configuration focuses the light beyond the sample stage, so the light incident on the sample is only slightly converging. However, because the focal lengths are so large and spot sizes so small, the light can be assumed to be collimated at the sample by invoking the small angle approximation [35]. This results in a laser spot size at the sample of approximately 1.5 mm in diameter.

## **Focused CASI Beam**

Most samples analyzed using the CASI can easily accommodate a 1.5 mm spot size. However, if the 0.325 mm by 0.2mm AFM-patterned area produced in this work was illuminated by a spot of this size, the patterned area would be overfilled by over 25 times at normal incidence (and more so at higher incident angles). Generating a BSDF of only the patterned area required the spot size to be reduced to a point where it could be completely contained within the patterned area.

Significant reductions in spot size were achieved by adjusting the position of the CASI's objective. This pulled the focal point back from the detector, towards the sample. The approximate size of the laser spot at the sample was determined using a graduated set of pinholes held in the sample mount. Passage through the pinhole was verified using the detector through comparison with the unobstructed power. The largest detector aperture was required for this measurement because the beam was no longer focused at the detector. The smallest spot size achieved through adjusting the objective only was still significantly larger than the patterned area.

Additional reductions in spot size were achieved through the use of a 3-inch diameter, converging, 500-mm focal length lens. This lens was suspended in the beam path between the source box and sample. Adjusting the objective position focused the beam through a 140- $\mu$ m pinhole. Because the light from the turning mirror was already converging, the effective focal length of the lens was reduced, enabling it to fit within the 500-mm long detector arm.



A framework was constructed from aluminum beams, corner brackets and angle brackets and bolted to the optical table to suspend the lens without obstructing the detector. Fine adjustments to the lens position were made by mounting the lens to two orthogonal micrometers. Hanging the lens on the end of a cantilever beam in this manner makes it susceptible to the vibrations induced by the abrupt movements of the CASI detector arm. A stable beam is especially critical when working with very small sample sizes. Vibrations are prevented by the high bending moment of the framework beams and the extensive corner bracing. The focused configuration is shown in Figure 18.

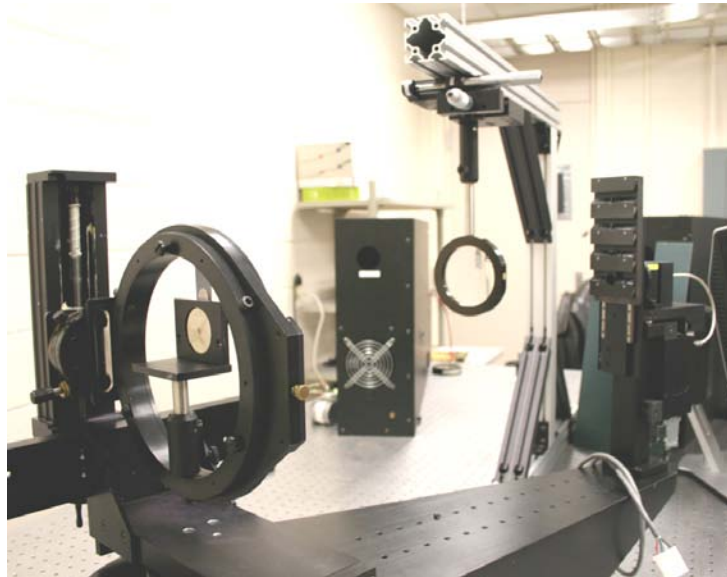


Figure 18: Focused CASI laser configuration (on patterned sample)

Once the beam is focused through the pinhole, the pinhole is removed and replaced with the sample mount and sample. The laser is centered on the patterned area through adjustments made to the X and Y axes of the rotation stage. Because the sample is so small, this process requires additional sample magnification. A hand-held microscope (10X magnification), mounted in an adjustable stand is sufficient. This is

only safe if used at high angles of incidence because very little light is reflected back toward the microscope in this condition. High incident angles are also necessary to observe beam walk. Beam walk refers to the increase in the projected area of the beam at high incident angles. Adjust the X, Y, and Z axes until the beam elongates symmetrically on both sides. When additional sample illumination was required, a fiber optic work light was used. The magnification apparatus is shown in Figure 19.



Figure 19: Magnification apparatus for centering CASI laser on patterned area.

## **Summary**

The layout and components of the CASI system were briefly covered. Modifications from normal operation, required for the analysis of small samples, were also described. These included the addition of a focusing optic suspended inside the detector arc and adjustments to the focus stage.

## **V. CASI Results**

### **Chapter Overview**

This chapter presents the results from the CASI experiments. Scatter from a 10- $\mu\text{m}$  AFM standard was collected in both the normal (detector-focused) and sample-focused laser configurations at 17 incident angles. These angles were repeated in the sample-focused condition on un-patterned polystyrene and again for AFM-patterned polystyrene. The AFM-patterned polystyrene was analyzed with the long axis of the sample parallel and perpendicular to the incoming beam. All experiments were conducted with both s- and p-polarized incident light.

The AFM standard produced many diffraction orders that were in good agreement with those predicted by the grating equation. Un-patterned polystyrene showed no significant scatter features other than a specular reflection. AFM-patterned polystyrene produced a broad -1 diffraction order at higher incident angles and a small resonant peak at only one incident angle for both 633- and 544-nm incident wavelengths.

### **CASI Measurements**

The layout, components, and normal operation of the CASI have already been discussed, as well as the procedures involved for focusing the beam to prevent overfilling the sample. Scattering measurements were conducted on three different surfaces: an AFM standard, un-patterned polystyrene, and patterned polystyrene.

The AFM standard (Figure 20) is a sample with well-known and well-defined surface features, normally used for calibrating an AFM. Its surface is an array of square

wells,  $5\mu\text{m}$  on a side and  $200\text{ nm}$  deep, with a period of  $10\mu\text{m}$ . The AFM standard is approximately  $5\text{ mm}$  in size, large enough to prevent overfilling by the laser spot size ( $1.5\text{ mm}$ ) even when the CASI is in the normal (detector-focused) configuration.

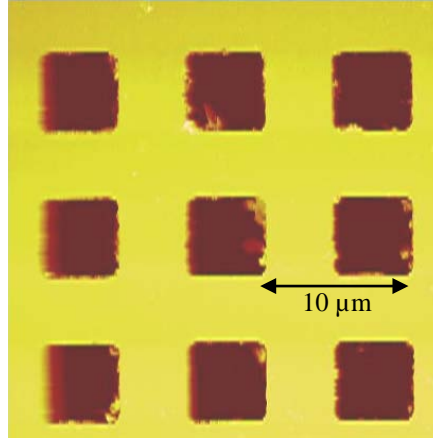


Figure 20:  $10\mu\text{m}$  AFM calibration standard (AFM image)

The AFM standard was analyzed in two CASI conditions, with the beam focused at the detector (normal configuration) and with the beam focused at the sample (for use with small samples). This was done to verify that departing from normal CASI operation by focusing the beam at the sample did not significantly impact the resulting scattering behavior. The experiment was conducted at two wavelengths:  $633\text{ nm}$  and  $544\text{ nm}$ . At  $633\text{ nm}$ , 17 angles of incidence ( $\theta_i$ ) ranging from  $0^\circ$  (normal incidence) to  $80^\circ$  (in steps of  $5^\circ$ ) were investigated. To confirm the results at  $633\text{ nm}$  (and also to save time) only five incident angles ( $0^\circ$  to  $80^\circ$ , steps of  $20^\circ$ ) were repeated at  $544\text{ nm}$ .

Figure 21(a) shows the results from  $\theta_i = 40^\circ$  at  $633\text{ nm}$ . The zero-order (specular) peak is seen at  $\theta_r = 40^\circ$ , along with five positive and 25 negative diffraction orders. This accounts for all 30 of the reflection diffraction orders predicted by the grating equation,

$m\lambda = d(\sin \theta_r - \sin \theta_i)$  [37]. In the detector-focused configuration, the -20<sup>th</sup> and -21<sup>st</sup> orders are blocked when the detector passes in front of the CASI source box (occlusion zone). In the sample-focused configuration, the 19<sup>th</sup> order is blocked as well because the additional optic extends slightly beyond the detector. Figure 21(b) shows the center section of Figure 21(a) in greater detail, clearly showing the close agreement between both CASI laser conditions.

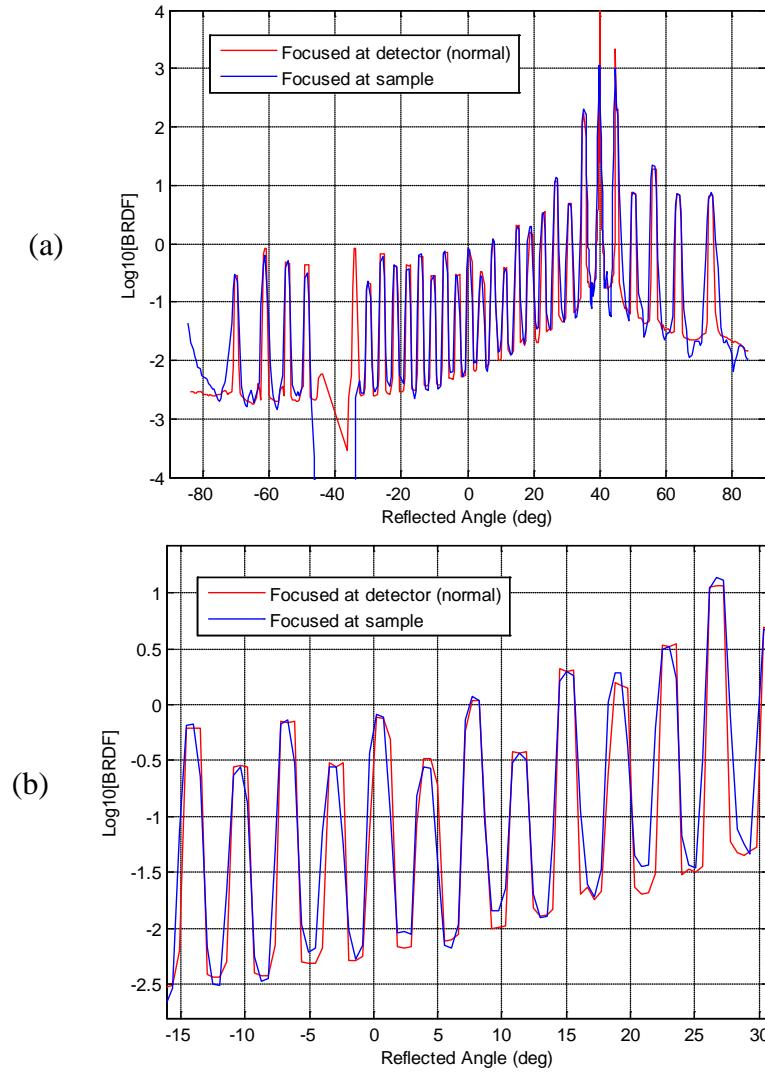


Figure 21: (a) Comparison between CASI laser focused at detector and sample, 10  $\mu\text{m}$  AFM standard,  $\theta_i = 40^\circ$ , p-polarization, 633 nm (b) zoomed in

Figure 22 (a) shows the results from  $\theta_i = 40^\circ$  at 544 nm. The zero-order (specular) peak is seen at  $\theta_r = 40^\circ$ , along with the six possible positive orders. All 30 negative diffraction orders are detected as well, though higher order peaks are less intense. The larger occlusion zone of the focused condition is also clearly seen. Figure 22(b) shows a section of Figure 22(a) in greater detail, clearly showing the close agreement between both CASI laser conditions at 544 nm.

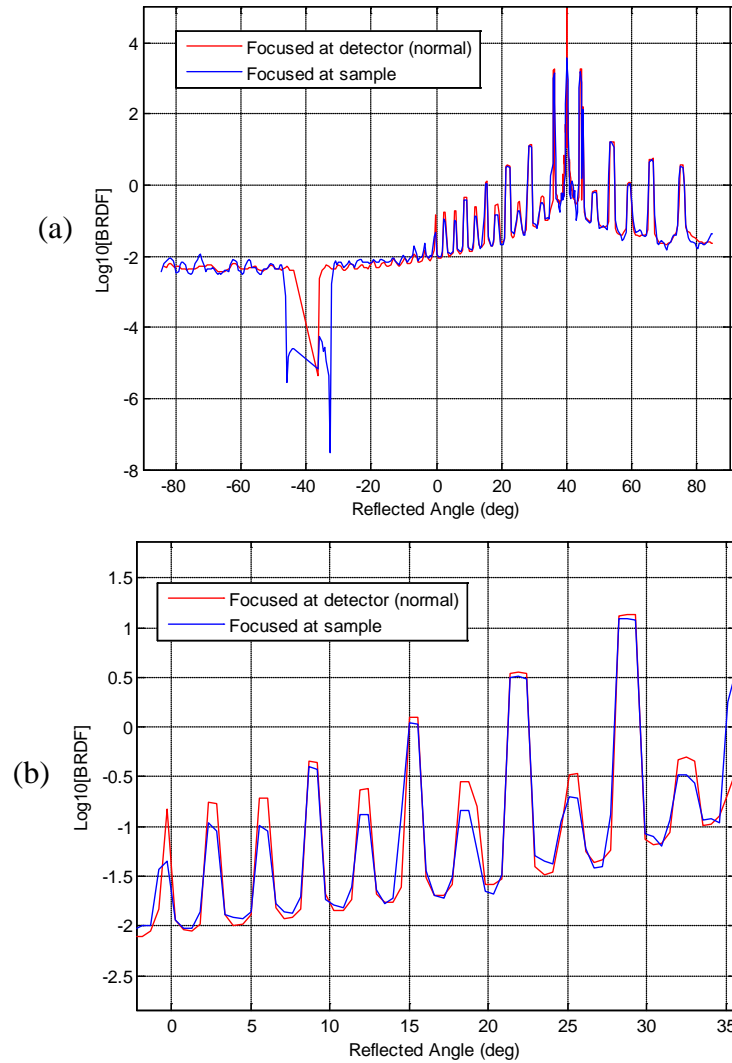


Figure 22: (a) Comparison between CASI laser focused at detector and sample, 10  $\mu\text{m}$  AFM standard,  $\theta_i = 40^\circ$ , p-polarization, 544 nm (b) zoomed in

These results indicate that there is little difference between operating the CASI with the laser focused at the detector or at the sample. Decreasing the spot size diameter from approximately 1.5 mm (unfocused) to 140  $\mu\text{m}$  (focused) increased the calculated beam divergence at the detector by approximately one order of magnitude (from 0.27 mm to 2.8 mm diameter, calculations in Appendix B). This increased the divergence angle from  $0.031^\circ$  to  $0.33^\circ$ , still within the realm of the small angle approximation [38]. Furthermore, the increased detector spot size (2.8 mm) also did not affect the results because it was still smaller than the aperture used for CASI data collection (14 mm). All results presented from this point onward were obtained with the laser focused at the sample.

All experimental data for the AFM standard was collected with both s- and p-polarized sources. The polarization had little effect, a result that was expected because the AFM standard is identical in both surface dimensions. Small differences in intensity between the polarizations may be due to slight differences in laser alignment introduced when the polarizations are changed. A comparison between polarizations is shown in Figure 23.

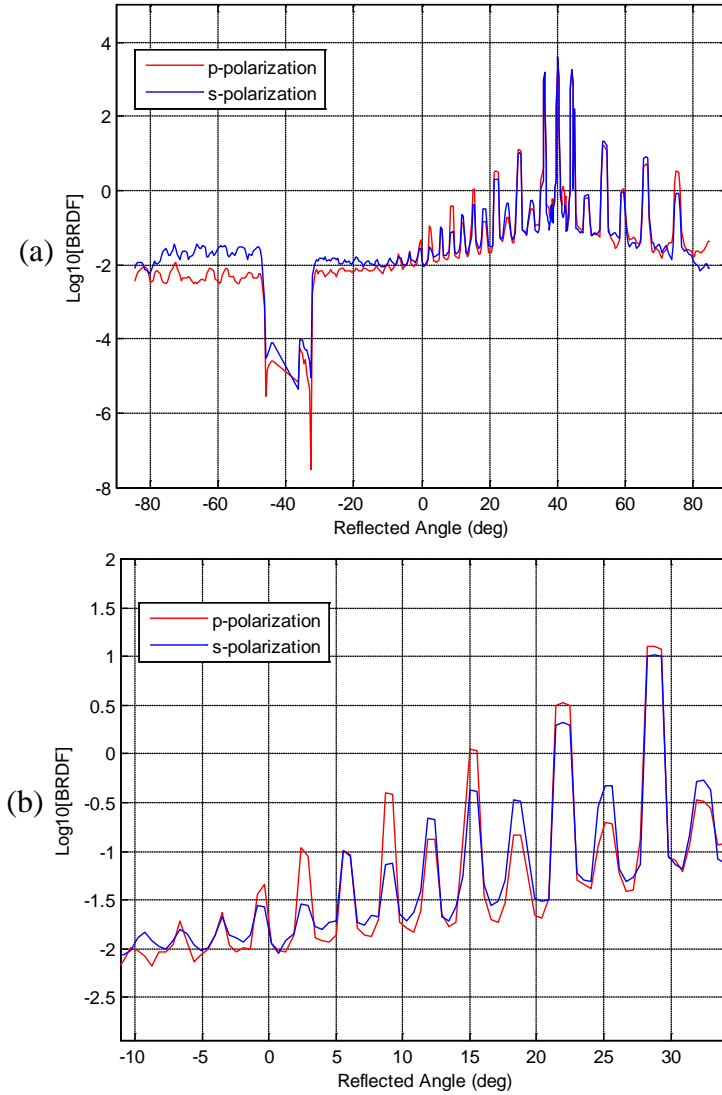


Figure 23: (a) Comparison between s- and p-polarization, 10- $\mu\text{m}$  AFM standard,  $\theta_i = 40^\circ$ , p-polarization, 544 nm, focused at sample (b) zoomed in

It was previously noted that the number of diffraction peaks detected agreed with those predicted by the grating equation ( $m\lambda = d(\sin \theta_r - \sin \theta_i)$ ). The locations of the peaks detected are also in very good agreement with the predicted locations. The fit between the equation and the CASI data for both 633 and 544 nm at  $\theta_i = 40^\circ$  is shown in



Figure 24. This comparison is made with data obtained with the CASI laser focused at the detector (normal). However, as shown above, the peak locations for both conditions are the same.

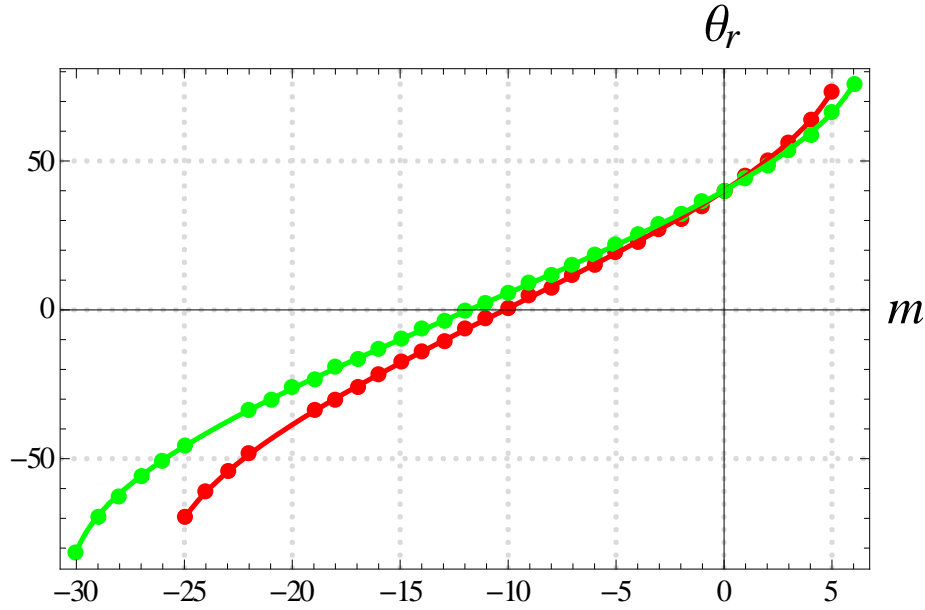


Figure 24: Fit between diffraction angles predicted by grating equation and experimentally obtained diffraction angles (at corresponding diffraction orders) for 10- $\mu$ m AFM standard grid, p-polarization (focused at detector) at  $\theta_i = 40^\circ$  for 633 nm (red) and 544 nm (green).

An un-patterned section of the polystyrene sample was analyzed to serve as a control. This section was located approximately 1 mm away from the patterned area. The same 17 incident angles were investigated as with the 10- $\mu$ m AFM standard. Representative data for  $\theta_i = 40^\circ$  is shown in Figure 25. Un-patterned polystyrene shows no distinguishable scattering features apart from the specular peak at  $40^\circ$  and the occlusion zone at  $-40^\circ$ . Un-patterned polystyrene also shows no strong polarization dependence.

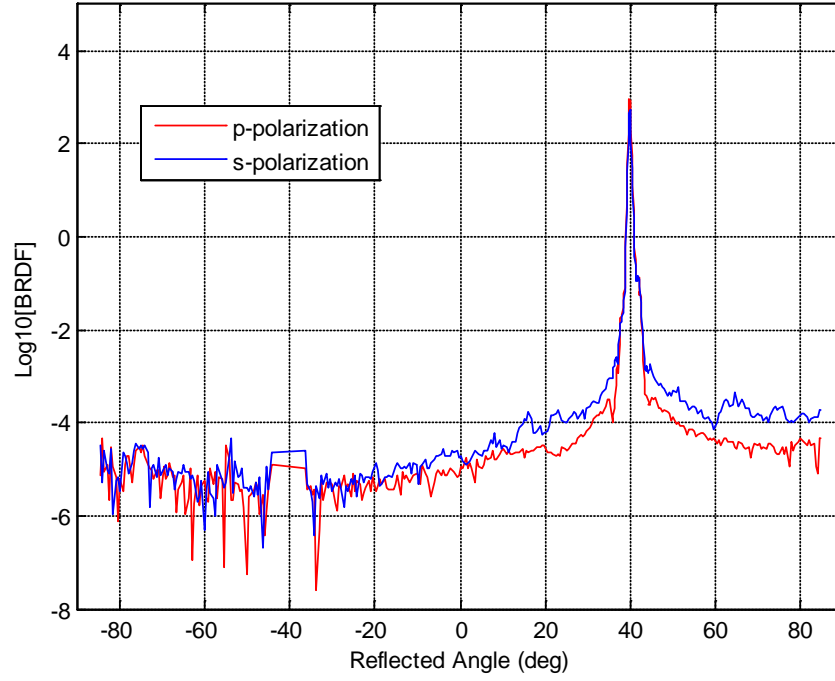
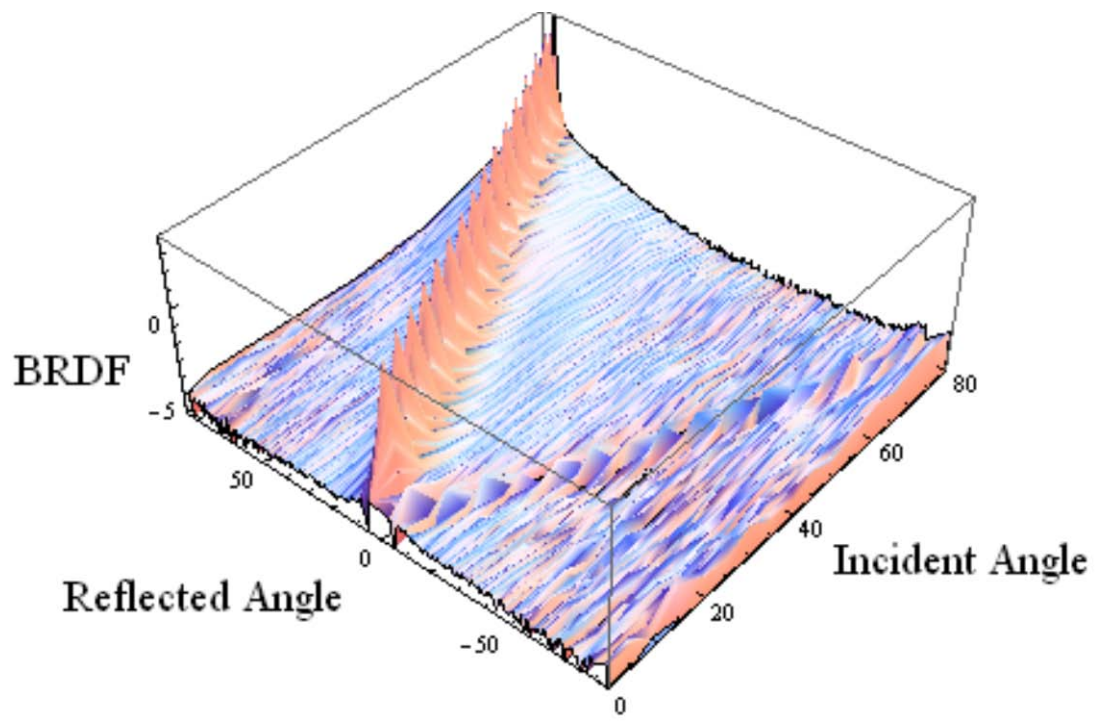
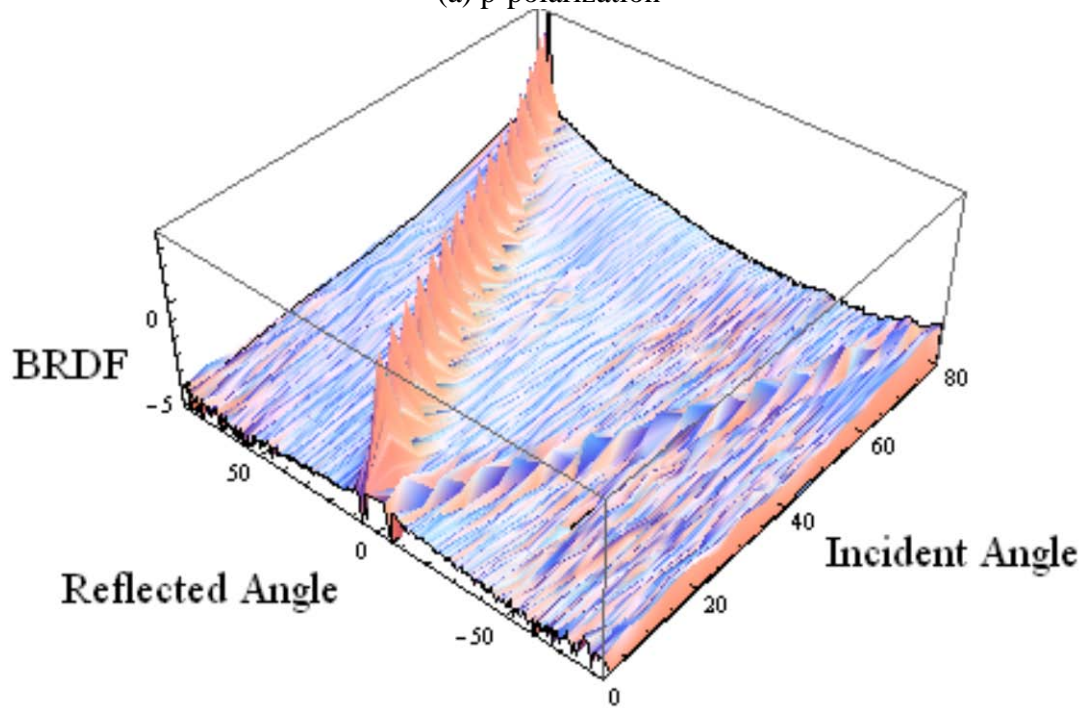


Figure 25: Un-patterned polystyrene control,  $\theta_i = 40^\circ$ , 633 nm.

Un-patterned polystyrene also shows no significant scatter features other than the specular peak at the other incident angles investigated (at both polarizations). This is easily seen in the 3D plots in Figure 26. Each incident angle shows only the specular peak and the occlusion zone. Un-patterned polystyrene was investigated at 633 nm only.



(a) p-polarization



(b) s-polarization

Figure 26: 3-D plot of  $\text{Log}_{10}[\text{BRDF}]$  vs.  $\theta_i$  and  $\theta_r$  for the polystyrene surface, 633 nm.

### Patterned Sample - 633 nm

The AFM-patterned polystyrene surface was analyzed at both 633 and 544 nm and at both s- and p-polarizations. The experimental setup is discussed in Chapter IV. 3D plots of the data for 633 nm are shown in Figures 27(a) (p-polarization) and (b) (s-polarization). This data was collected with the long (325  $\mu\text{m}$ ) axis of the patterned area parallel with the incoming laser beam. In addition to the familiar specular peak and occlusion zone, a -1 diffraction order appears for  $\theta_i \geq 40^\circ$ . An additional small feature appears *only* at  $\theta_i = 40^\circ$  as well. It should be noted that all peaks appear broader at their bases because of the interpolation of the software used to generate the 3D figure.

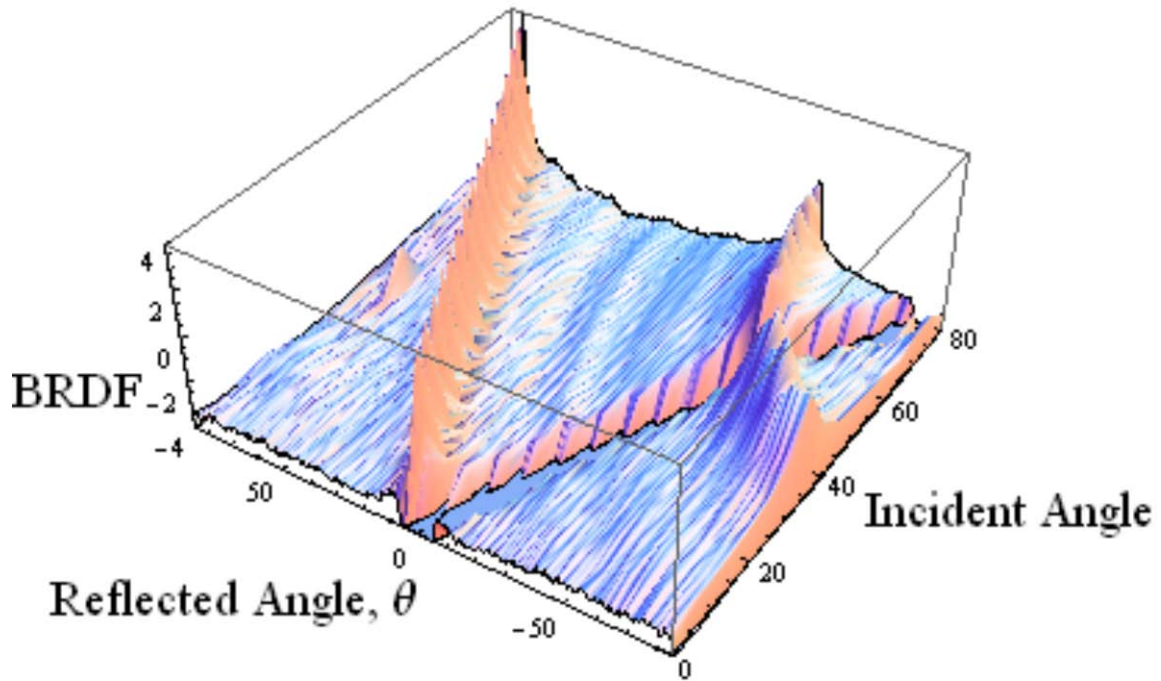
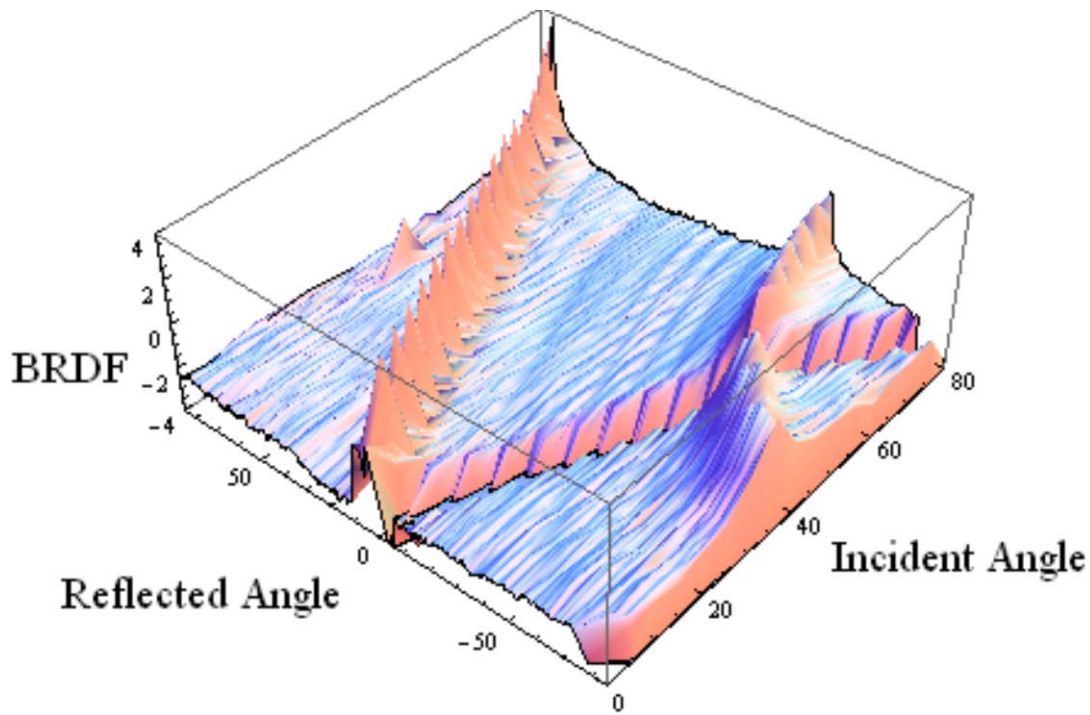


Figure 27(a): p-polarization



(b) s-polarization

Figure 27: 3-D plot of  $\text{Log}_{10}[\text{BRDF}]$  vs.  $\theta_i$  and  $\theta_r$  for the patterned sample, 633 nm, long axis of pattern parallel to incoming laser

The relationship between the experimental angular location of the  $m = -1$  diffraction peak and incident angle is shown in Figure 28. Also shown is the relationship between incident angle and reflected angle according to the classic grating equation (for  $m = -1$ ,  $\lambda = 633 \text{ nm}$ ,  $d = 400 \text{ nm}$ ). The missing data point at  $50^\circ$  is due to the detector occlusion zone. The data point at  $55^\circ$  is included but may be suspect because it was gathered on the edge of this zone. The fit between the two is excellent, strongly supporting the identification of those peaks as the -1 diffraction order peaks.

It should also be noted that the nature of the -1 diffraction peaks for the patterned sample are not well-defined spots (like the AFM standard). They show a definite

maximum, but also present is considerable finer structure, presumably caused by slight feature non-uniformity and the triangular shape of the indentations (shown in Figure 29).

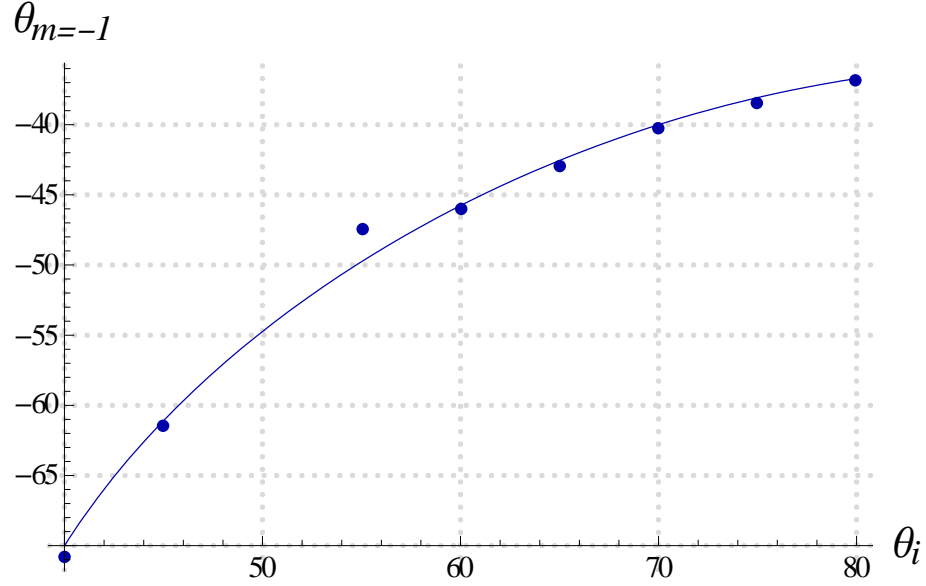


Figure 28: Fit between  $m=-1$  diffraction order at different  $\theta_i$  predicted by grating equation ( $m\lambda = d(\sin \theta_r - \sin \theta_i)$ ) and experimentally obtained diffraction angles for patterned sample, p-polarization, 633 nm.



Figure 29: Diffraction pattern for AFM-patterned sample

The BRDF of the patterned sample at  $\theta_i = 40^\circ$  is shown in Figure 30, showing the specular peak, -1 diffraction order, and an additional small feature, which is present at

70.27°. It is present at both incident polarizations. It does not appear to be an experimental artifact or to be caused by the large-scale periodicity of the “tiles” used in the patterning technique. This is confirmed by rotating the patterned sample 90° and collecting the same data set as for the original configuration (long axis parallel to incoming beam). The BRDF from both the original and rotated orientations at  $\theta_i = 40^\circ$  is shown in Figure 31. This strengthens the case that the peak is due to the generated pattern, and even though its exact cause at this point is unknown, a promising hypothesis is that it is due to a guided resonant mode. For more information on the unique scatter peaks produced for only one incident angle, see [4].

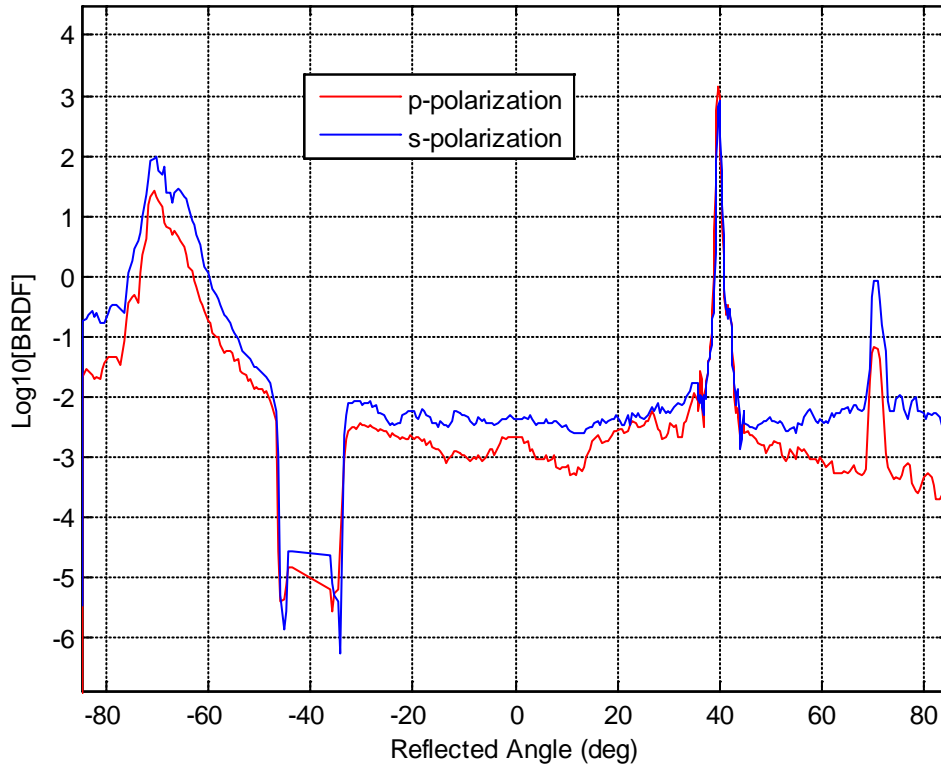


Figure 30: Patterned polystyrene,  $\theta_i = 40^\circ$ , showing expanded view of additional feature at 70.27°, normal pattern orientation only, both polarizations, 633 nm.

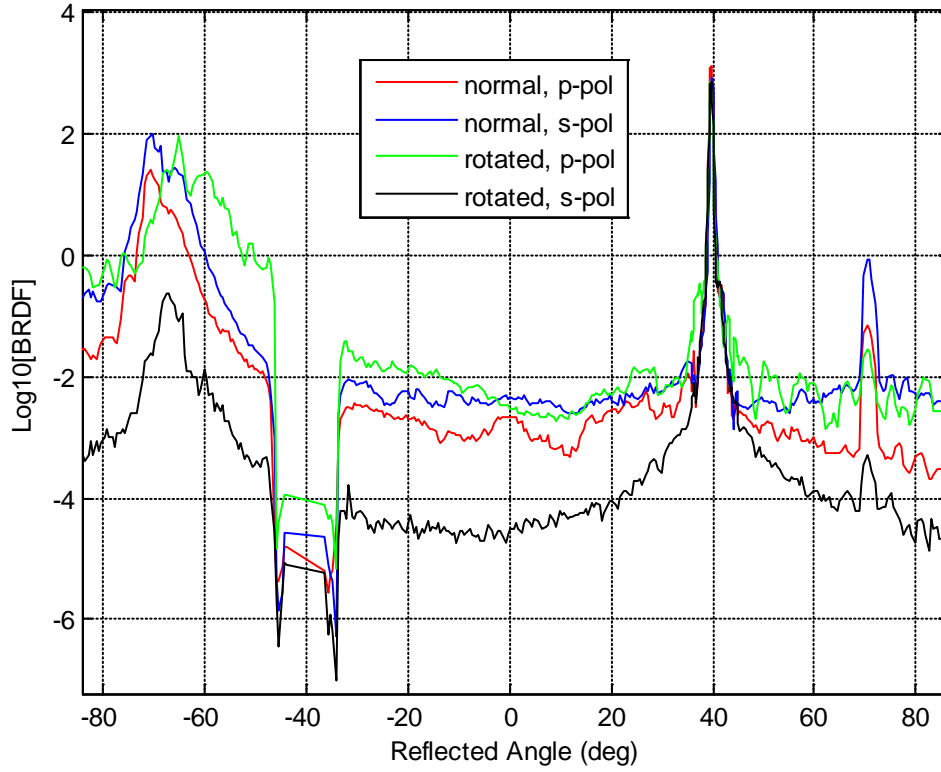
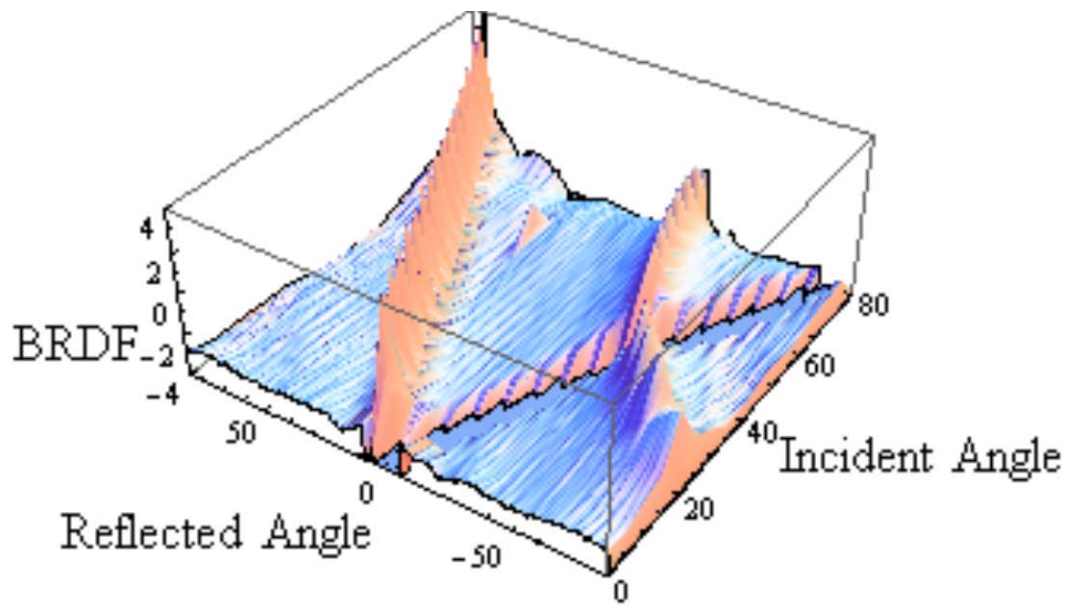


Figure 31: Patterned polystyrene,  $\theta_i = 40^\circ$ , showing expanded view of additional feature at  $70.27^\circ$ , both pattern orientations, both polarizations, 633 nm.

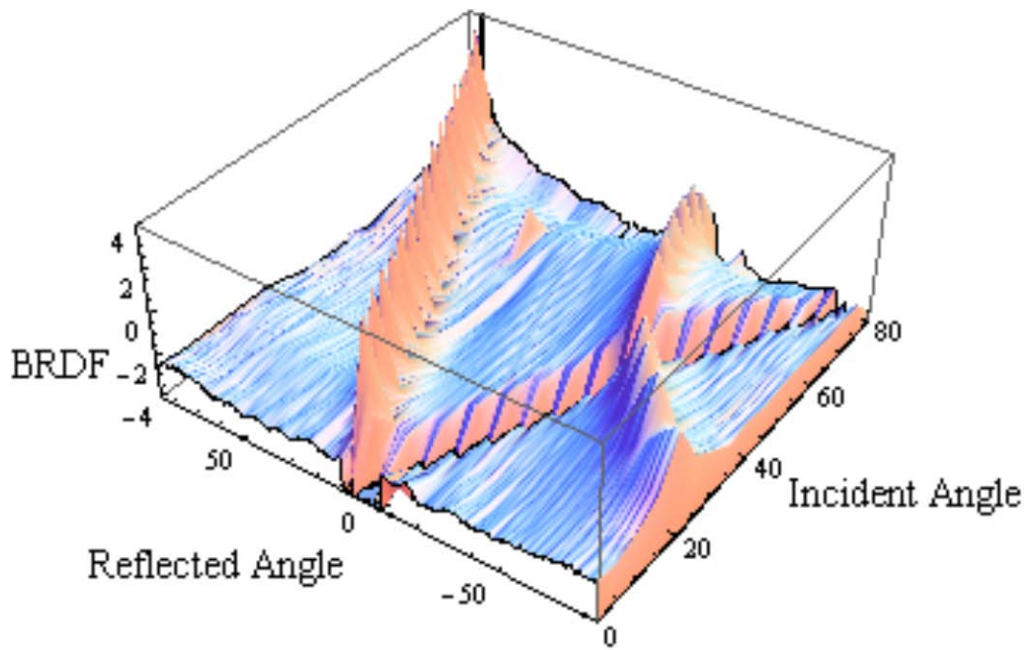
### Patterned Sample – 544 nm

The AFM-patterned sample was also analyzed by the CASI at 544 nm. 3-D plots of the data at the same 17 incident angles are shown in Figure 32. Like those obtained at 633 nm, the results at 544 nm contain specular reflections, as well as -1 diffraction orders. However, the diffraction orders first appear at a lower incident angle (consistent with the diffraction grating equation). The small resonant feature that appeared at  $70.27^\circ$  ( $\theta_i = 40^\circ$ ) in the 633 nm results is shifted to  $28.8^\circ$  ( $\theta_i = 60^\circ$ ) in the 544 nm results. Again, this is consistent with identifying it as due to guided mode resonance. A 2-D plot of the data from  $\theta_i = 60^\circ$  shows a more detailed view of this peak, at both polarizations (Figure 33).





(a) p-polarization



(b) s-polarization

Figure 32: 3-D plot of  $\text{Log}_{10}[\text{BRDF}]$  vs.  $\theta_i$  and  $\theta_r$  for the patterned sample, 544 nm, long axis of pattern parallel to incoming laser

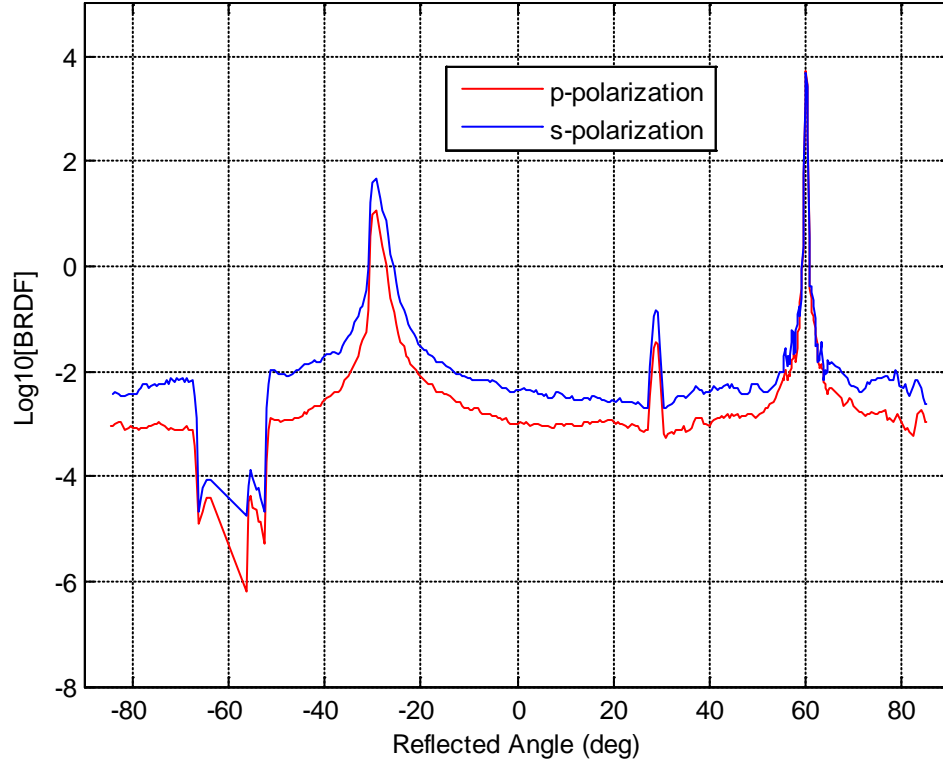


Figure 33: Patterned polystyrene,  $\theta_i = 60^\circ$ , showing additional feature at  $28.8^\circ$ , both polarizations, 544 nm.

In the same manner as with the additional feature at 633 nm, the sample mount was rotated  $90^\circ$  to rule out any effects due to large-scale “tile” periodicity. The results from this experiment are shown in Figure 34. As before, the small resonant feature remains.

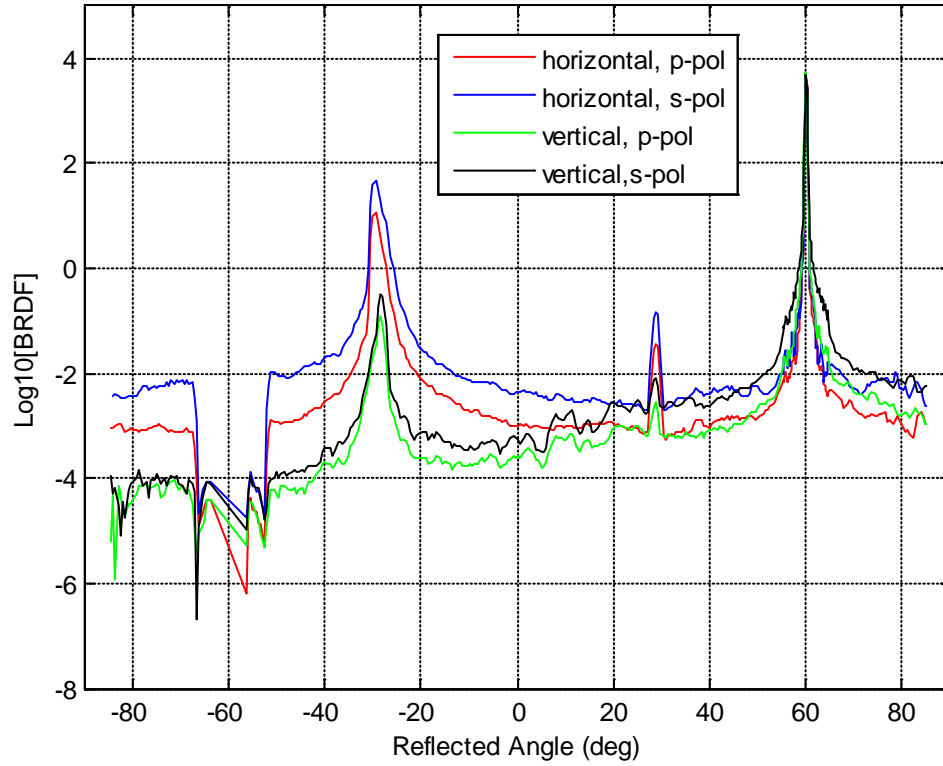


Figure 34: Patterned polystyrene,  $\theta_i = 60^\circ$ , showing additional feature at  $28.8^\circ$ , both pattern orientations, both polarizations, 544 nm.

### Investigative Questions Answered

The CASI results clearly show that surface features were created that were able to diffract incoming light in a manner consistent with established theory. This supports the identification of this material as a photonic crystal. The locations of the -1 diffraction orders at corresponding incidence angles independently verify the small-scale surface periodicity of 400 nm. CASI modifications to reduce the beam spot had little effect on results, validating its future use for small samples.

## Summary

This chapter presented the results from CASI experiments on three surfaces (AFM standard and patterned/un-patterned polystyrene) at two wavelengths (633 and 544 nm). Data from the AFM standard confirmed that results were unaffected by focusing the laser beam. Un-patterned polystyrene showed little significant scatter other than the specular reflection lobe. AFM-patterned polystyrene showed a -1 diffraction order at high incident angles and one resonant peak at one incident angle for both wavelengths. All diffraction data was in agreement with the diffraction grating equation.

## **VI. Conclusions and Recommendations**

### **Chapter Overview**

This chapter summarizes the findings of this research and comments on its significance. Also covered are more short-term immediate actions to be taken and longer term recommendations for future work.

### **Contributions of Research**

It had been previously demonstrated that the AFM was capable of generating a two-dimensional nanoscale array of surface features from a thin polymer film [24-25]. This AFM-patterning work improved on those efforts in several ways. First, the size of an individual array was greatly increased (from 3 x 3  $\mu\text{m}$  to 60 x 80  $\mu\text{m}$ ). The height of the surface features within the array was increased as well (from < 10  $\mu\text{m}$  to 140  $\mu\text{m}$ ), increasing their ability to interact with incoming light. The pitch of the array was larger (from 120 nm to 400 nm), but this could be reduced by using a sharper AFM tip. Secondly, individual patterned arrays were “tiled” together to generate a much larger composite array (325  $\mu\text{m}$  x 200  $\mu\text{m}$ ).

The composite AFM-patterned surface was large enough to permit optical scattering measurements to be conducted using the AFIT’s Complete Angle Scatter Instrument (CASI). This required the CASI beam spot size at the sample to be greatly reduced through the use of an additional lens located between the CASI source box and the sample. Calibration experiments with an AFM standard showed that this modification had little effect on scatter measurements.

The BRDFs (bi-directional distribution functions) of the AFM-patterned sample showed a -1 diffraction order at high angles of incidence, consistent with prior CASI analysis of known photonic crystal samples [4]. Also present at both wavelengths investigated (544 and 633 nm) was a small resonant peak, present at both s- and p-polarizations. This peak remained even after a 90° pattern rotation. The exact cause of this resonance is currently unknown, but it is presumed to be due to a guided mode resonance of the AFM-patterned structure [4].

### **Significance of Research**

This research explores an AFM-based alternative to current lithographic techniques to fabricate the small features required by photonic crystals (PCs) and negative index metamaterials (NIMs). It also demonstrates the ability of existing scattering instruments to characterize very small samples of these new materials with little loss in data quality. This nano-patterning technique may be extended in a low-cost, low-tech alternative through the development of 1D knife edges or combs used in place of the AFM tip or the development of a template-driven technique utilizing force (as in this work) or elevated temperatures for surface patterning.

### **Recommendations for Action**

Determine what the cause of the resonant peak is. This author has investigated diffraction from large-scale tile periodicity, blazing from the interior faces of the indentations, and waveguide coupling unsuccessfully. The existence of resonance at only one incident angle is the most difficult detail to explain.

Reverse the relative indices of the film and substrate materials. In the sample used here, the refractive index of the silicon substrate was significantly higher ( $n \approx 3.4$ ) than the polystyrene film ( $n \approx 1.5$ ). This allowed any light in the surface film to leak into the substrate (since there is no efficient interface reflection or critical angle). Using a substrate with a lower refractive index would reduce this of loss.

Determine a way to focus the CASI's IR wavelengths. At these wavelengths, the surface features generated here would be substantially sub-wavelength (less than  $\lambda/2$ ) and the response of this material in this regime should be investigated.

Modify a spectrophotometer to focus its incident light (or scale up the material) so that the (reflective) response of the material can be investigated in wavelength-space. Alternatively, generating a similar pattern on a transparent substrate would allow transmission experiments. This would identify any maxima (reflection) or minima (transmission) wavelength response, similar to those in a guided mode resonance filter (GMRF), and save considerable time in CASI measurements by indicating which specific angles should be investigated.

Optimize the AFM control to generate these features at a faster rate. Shorten the dwell time between indentations and optimize the scan range and z scan start. The development of a composite (multiple tips) diamond AFM tip would allow the creation of multiple indentations simultaneously (though this would impose predetermined feature spacing).

## Recommendations for Future Research

Future possibilities exist for modifications to AFM-patterned surface arrays. The surface produced here was left open and used air ( $n \approx 1$ ) as the filler between the polystyrene surface features. Future work could explore techniques for backfilling these surface features with materials of varying indices. Alternatively, the surface could be left open and used as a template to properly space metallic nano-particles. This could allow the magnetic permeability ( $\mu$ ) of the material to be manipulated, which would be similar to the approach employed by Grigorenko *et al.* [39] wherein they use pairs of electromagnetically coupled nano-dot posts to produce negative  $\mu$ . The spacing of the posts used is 400 nm and the size is similar to the size of the nano-indentations produced in this work. Perhaps these post pairs could be replaced by spherical gold nano-particles laid down using the patterned surface as a nano-template.

## Summary

The two-dimensional array of polystyrene surface features covered here was produced using an AFM and was shown to behave like a photonic crystal. This has potential application in the future fabrication of these materials and is the first time a photonic crystal has been demonstrated to be produced by AFM surface nano-patterning.



## Appendix A

### MATLAB code for importing and plotting 2-D figures

```
%File reads in and plots two .txt CASI files
fid=fopen('data_file_name1.txt');
A1=textscan(fid,'%s',96); %read in file header
B1=textscan(fid,'%n %n %n'); %read in 3 columns of data

fid=fopen('data_file_name2.txt');
A2=textscan(fid,'%s',96);
B2=textscan(fid,'%n %n %n');

plot(B1{2},log10(B1{3}), 'LineWidth',1, 'Color', 'b');
%plots BRDF vs. reflected angle, relative to sample normal
hold on;
plot(B2{2},log10(B2{3}), 'LineWidth',1, 'Color', 'r')

%graph formatting
grid on;
xlabel('Reflected Angle (deg)');
ylabel('Log10[BRDF]');
legend('label_one', 'label_two');
```

## Mathematica code for importing and plotting 3D figures

```
(*For this code to work as written, the files must be named
   "Specular XX Degrees Two Apertures ppol.txt"
Changes can be made, but the incident angle must be in the title.  The
loops are written to cycle from 0 to 80 degrees incident (by 5
degrees).*)
```

```
ClearAll[datatwoangles,datatwoangletable,datatwoangleplot]
```

```
datum="L:\\Directory Path\\";
offset=23;
jcount=0;
Do[
  Do[
    {
      If[8==degrees2&&5==degrees1,,
        {datatwoangles[degrees2,degrees1]=Import[StringJoin[datum,{"Specular "
          ,ToString[degrees2],ToString[degrees1]," Degrees Two Apertures
          ppol.txt"}],"Table"],jcount=jcount+1}]}
      ,{degrees1,0,5,5}]
      ,{degrees2,0,8,1}]
```

```
datatwoangleplot:=datatwoangletable[0,0];
```

```
Do[
  Do[
    If[8==degrees2&&5==degrees1,,
      {datatwoangletable[degrees2,degrees1]=
        Table[{degrees2*10+degrees1,datatwoangles[degrees2,degrees1]
          [[i,2]],Log[10,datatwoangles[degrees2,degrees1]][[i,3]]},
          {i,offset,Length[datatwoangles[degrees2,degrees1]],1}},
        datatwoangleplot=Join[datatwoangleplot,
          datatwoangletable[degrees2,degrees1]]}]
      ,{degrees1,0,5,5}]
      ,{degrees2,0,8,1}]
```

```
ListPlot3D[datatwoangleplot,Mesh->None,InterpolationOrder->5,
  PlotRange->{{0,80},{-85,85},{-4,4}},
  AxesLabel->{Text[Style["Incident Angle",FontSize->18]],
    Text[Style["Reflected Angle,  $\theta$ ",FontSize->18]],
    Text[Style["BRDF",FontSize->18]]}]
```

```
(*Thank you to Shawn Hackett for providing this Mathematica code*)
```

## Appendix B

### Beam divergence calculations

$$2\theta_0 = \frac{4}{\pi} \frac{\lambda}{2W_0}$$

$\theta_0$  = beam divergence half-angle (radians)

$\lambda$  = wavelength (m)

$W_0$  = beam waist radius (m)

$$\tan \theta_0 = \frac{R_s}{l}$$

$R_s$  = radius of spot size at detector

$l$  = distance from sample to detector

*Sample Calculation (focused):*

$$2\theta_0 = \frac{4}{\pi} \frac{633nm}{2(70\mu m)} = 0.00576 \text{ radians}$$

$$\theta_0 = 0.00288 \text{ radians}$$

$$\tan(0.00288) = \frac{R_s}{0.5m}$$

$$R_s = 1.4 \text{ mm}$$

## Bibliography

- [1] J. D. Joannopoulos, R. D. Meade, and J. N. Winn, *Photonic Crystals: Molding the Flow of Light*, Princeton University Press, 1995.
- [2] Fuchyi Yang, Gary Yen, and Brian T. Cunningham, "Voltage-tuned resonant reflectance optical filter for visible wavelengths fabricated by nanoreplica molding," *Applied Physics Letters*, vol. 90, pp. 261109, 2007.
- [3] Fuchyi Yang, Gary Yen, Gilles Rasigade, Julio A. N. T. Soares, and Brian T. Cunningham, "Optically tuned resonant optical reflectance filter," *Applied Physics Letters*, vol. 92, pp. 091115, 2008.
- [4] Robert B. Lamott, "Analysis and Application of the Bi-directional Scatter Distribution Function of Photonic Crystals," Air Force Institute of Technology, Dayton, OH, Thesis 2009.
- [5] I. Prieto, B. Galiana, P. A. Postigo, C. Algora, L. J. Martínez, and I. Rey-Stolle, "Enhanced quantum efficiency of Ge solar cells by a two-dimensional photonic crystal nanostructured surface," *Applied Physics Letters*, vol. 94, pp. 191102, 2009.
- [6] Valery Shklover, Leonid Braginsky, Gregoire Witz, Matthew Mishrikey, and Christian Hafner, "High-Temperature Photonic Structures. Thermal Barrier Coatings, Infrared Sources and Other Applications," *Journal of Computational and Theoretical Nanoscience*, vol. 5, pp. 862-893, 2008.
- [7] Alexandra Boltasseva and Vladimir M. Shalaev, "Fabrication of optical negative-index metamaterials: Recent advances and outlook," *Metamaterials*, vol. 2, pp.1-17, 2008.
- [8] Peter Vukusic, "Manipulating the flow of light with photonic crystals," *Physics Today*, pp. 82-3, Oct 2006.
- [9] D. Smith, J. Pendry, and M. Wiltshire, "Metamaterials and Negative Refractive Index," *Science* [online], vol. 305, no. 5685, Aug 2004, accessed 21 Aug 2009.
- [10] Allan Greenleaf, Yaroslav Kurylev, Matti Lassas, and Gunther Uhlmann, "Electromagnetic Wormholes and Virtual Magnetic Monopoles from Metamaterials," *Physical Review Letters*, vol. 99, pp. 183901, 2007.
- [11] Kosmas L. Tsakmakidis and Ortwin Hess, "Watch your back," *Nature*, vol. 451, pp. 27, 3 Jan 2008.

- [12] D. Schurig, J. J. Mock, B. J. Justice, S. A. Cummer, J. B. Pendry, A. F. Starr, D. R. Smith, "Metamaterial Electromagnetic Cloak at Microwave Frequencies," *Science*, vol. 314, no. 5801, pp. 977-980, 2006. (abstract only)
- [13] Wenshan Cai, Uday K. Chettiar, Alexander V. Kildishev, and Vladimir M. Shalaev, "Optical cloaking with metamaterials," *Nature Photonics*, vol. 1, pp. 224-227, 2007. (abstract only)
- [14] Wei Wu, Zhaoning Yu, Shih-Yuan Wang, and R. Stanley Williams, "Midinfrared metamaterials fabricated by nanoimprint lithography," *Applied Physics Letters*, vol. 90, pp. 063107, 2007.
- [15] Nils Feth, Manuel Decker, Gunnar Dolling, Matthias W. Klein, Stefan Linden, and Martin Wegener, "Photonic metamaterials – new opportunities for nanoimprint," *IEEE* (abstract only).
- [16] D. M. Eigler and E. K. Schweizer, "Positioning single atoms with a scanning tunneling microscope," *Nature*, vol. 344, pp. 524-526, 1990.
- [17] Ricardo Garcia, Ramsés V. Martinez, and Javier Martinez, "Nano-chemistry and scanning probe nanolithographies," *Chemical Society Reviews*, vol. 35, pp. 29-38, 2006.
- [18] Kathryn Wilder and Calvin F. Quate, "Noncontact nanolithography using the atomic force microscope," *Applied Physics Letters*, vol. 73, no. 17, pp. 2527-2529, 1998.
- [19] Gregory F. Meyers, Benjamin M. DeKoven, and Jerry T. Seitz, "Is the Molecular Surface of Polystyrene Really Glassy?" *Langmuir*, vol. 8, pp. 2330-2335, 1992.
- [20] D. D. Woodland and W. N. Unertl, "Initial wear in nanometer-scale contacts on polystyrene," *Wear*, vol. 203-204, pp. 685-691, 1997.
- [21] Z. Elkaakour, J. P. Aimé, T. Bouhacina, C. Odin, and T. Masuda, "Bundle Formation of Polymers with an Atomic Force Microscope in Contact Mode: A Friction Versus Peeling Process," *Physical Review Letters*, vol. 73, no. 24, pp. 3231-3234, 1994.
- [22] Taku Aoike, Takahiro Yamamoto, Hiroki Uehara, Takeshi Yamanobe, and Tadashi Komoto, "Surface Deformation Properties of Polystyrene as Evaluated from the Morphology of Surfaces Scratched by Using the Tip of a Scanning Force Microscope," *Langmuir*, vol. 17, pp. 5688-5692, 2001.
- [23] J. P. Pickering and G. J. Vancso, "On the formation of oriented nanometer scale patterns on amorphous polymer surfaces studied by atomic force microscopy," *Applied Surface Science*, vol. 148, pp. 147-154, 1999.

- [24] Guangming Li and Larry W. Burggraf, "Controlled patterning of polymer films using an AFM tip as a nano-hammer," *Nanotechnology*, vol. 18, no. 245302, 2007.
- [25] Guangming Li and Larry W. Burggraf, "Surface stress influences on nanopatterns formed in polystyrene films using a force-modulated nanohammer," *Nanotechnology*, vol. 19, no. 095301, 2008.
- [26] C. G. Parazzoli, R. B. Greegor, K. Li, B. E. C. Koltenbah, and M. Tanielian, "Experimental Verification and Simulation of Negative Index of Refraction Using Snell's Law," *Physical Review Letters*, vol. 90, no. 10, pp. 107401, 14 Mar 2003.
- [27] J. Pendry, "Positively negative," *Nature*, vol. 423, pp. 22-23, 1 May 2003.
- [28] Thomas M. Fitzgerald, "A Novel Optical Metamaterial Characterization Technique Based on Bidirectional Ellipsometry," Air Force Institute of Technology, Dayton, OH, Dissertation Prospectus 2009.
- [29] "Dimension V Instruction Manual," Veeco Instruments Inc., 004-997-000, 2008.
- [30] "Atomic\_force\_microscope\_block\_diagram.svg," [Online].  
[http://en.wikipedia.org/wiki/Atomic\\_force\\_microscope](http://en.wikipedia.org/wiki/Atomic_force_microscope)
- [31] "Nanoindentation and Nanoscratching with SPMs For NanoScope™ Version 5.30 Rev. 2 Software," Support Note No. 013-225-000, Rev. G, Veeco Inc. 2005
- [32] Shane Juhl, David Phillips, and Richard A. Vaia, "Precise formation of nanoscopic dots on polystyrene film using z-lift electrostatic lithography," *Applied Physics Letters*, vol. 85, pp. 3836-8.
- [33] "DNISP," [Online]. <https://www.veecoprobes.com/p-3253-dnisp.aspx>
- [34] "Complete Angle Scatter Instrument," Schmitt Measurement Systems, Inc. [Online].  
<http://www.schmitt-ind.com/pdf/casi.pdf>
- [35] Bradley Balling, "A Comparative Study of the Bi-Directional Reflectance Distribution Function of Several Surfaces as a Mid-wave Infrared Diffuse Reflectance Standard," Air Force Institute of Technology, Dayton, OH, Thesis 2009.
- [36] D. Maga, "CASI Operating Manual," Dept. of Engineering Physics, 2950 Hobson Way, WPAFB, OH 45431.
- [37] Eugene Hecht, *Optics*, 4th ed. San Francisco: Addison Wesley, 2002.

- [38] Bahaa E. A. Saleh and Malvin Carl Teich, *Fundamentals of Photonics*, 2nd ed. Hoboken: Wiley, 2007.
- [39] A. N. Grigorenko, A. K. Geim, H. F. Gleeson, Y. Zhang, A. A. Firsov, I. Y. Khrushchev, and J. Petrovic, "Nanofabricated media with negative permeability at visible frequencies," *Nature*, vol. 438, pp. 335-338, 2005.

REPORT DOCUMENTATION PAGE				Form Approved OMB No. 074-0188	
<p>The public reporting burden for this collection of information is estimated to average 1 hour per response, including the time for reviewing instructions, searching existing data sources, gathering and maintaining the data needed, and completing and reviewing the collection of information. Send comments regarding this burden estimate or any other aspect of the collection of information, including suggestions for reducing this burden to Department of Defense, Washington Headquarters Services, Directorate for Information Operations and Reports (0704-0188), 1215 Jefferson Davis Highway, Suite 1204, Arlington, VA 22202-4302. Respondents should be aware that notwithstanding any other provision of law, no person shall be subject to a penalty for failing to comply with a collection of information if it does not display a currently valid OMB control number.</p> <p><b>PLEASE DO NOT RETURN YOUR FORM TO THE ABOVE ADDRESS.</b></p>					
1. REPORT DATE (DD-MM-YYYY) 25-03-2010		2. REPORT TYPE Master's Thesis		3. DATES COVERED (From - To) Aug 2008 - March 2010	
4. TITLE AND SUBTITLE  AFM-Patterned 2-D Thin-Film Photonic Crystal Analyzed by Complete Angle Scatter				5a. CONTRACT NUMBER N/A	
				5b. GRANT NUMBER N/A	
				5c. PROGRAM ELEMENT NUMBER N/A	
6. AUTHOR(S)  Herr,Nicholas C., 2 Lt, USAF				5d. PROJECT NUMBER N/A	
				5e. TASK NUMBER N/A	
				5f. WORK UNIT NUMBER N/A	
7. PERFORMING ORGANIZATION NAMES(S) AND ADDRESS(S) Air Force Institute of Technology Graduate School of Engineering and Management (AFIT/EN) 2950 Hobson Way WPAFB OH 45433-7765				8. PERFORMING ORGANIZATION REPORT NUMBER  AFIT/GMS/ENP/10-M01	
9. SPONSORING/MONITORING AGENCY NAME(S) AND ADDRESS(ES) Dr. Richard Vaia Materials and Manufacturing Directorate Air Force Research Laboratory, Air Force Materiel Command Wright-Patterson AFB, OH 45433-7750				10. SPONSOR/MONITOR'S ACRONYM(S) AFRL/MLBP	
				11. SPONSOR/MONITOR'S REPORT NUMBER(S)	
12. DISTRIBUTION/AVAILABILITY STATEMENT  APPROVED FOR PUBLIC RELEASE; DISTRIBUTION UNLIMITED.					
13. SUPPLEMENTARY NOTES					
14. ABSTRACT <p>The purpose of this research was to use an atomic force microscope (AFM) to generate a 2-D square array of sub-wavelength surface features from a single material over a region large enough to permit optical characterization. This work is an extension of previous AFIT nano-patterning work and is in response to the small subunit sizes demanded for the production of optical metamaterials and photonic crystals. A diamond nano-indentation AFM probe was used to produce a 325-µm by 200-µm array of indentations in a 120-nm thick polystyrene film deposited on silicon. Indentation spacing of 400 nm produced well-defined surface features with a maximum height of 140 nm. The full size array was achieved by tiling together single arrays, limited in size by the AFM scanner range, through the use of the AFM's translation stage. A Complete Angle Scatter Instrument (CASI) was used (beam focused to 140 µm) to determine scatter at incident angles ranging from 0 to 80 degrees. Two wavelengths were investigated (633 and 544 nm) at both s and p-polarization. Negative first order diffraction peaks were observed for both wavelengths and were consistent with feature spacing. This is the first demonstration of an AFM-patterned surface to behave as a 2D photonic crystal and has potential DoD applications in laser eye protection, enhanced solar cell efficiency, satellite thermal management, and anti-reflection coatings for high power laser optics.</p>					
15. SUBJECT TERMS AFM, Nano-patterning, Photonic Crystal					
16. SECURITY CLASSIFICATION OF:			17. LIMITATION OF ABSTRACT	18. NUMBER OF PAGES	19a. NAME OF RESPONSIBLE PERSON
a. REPORT	b. ABSTRACT	c. THIS PAGE			Larry W. Burggraf, PhD
U	U	U	UU	88	19b. TELEPHONE NUMBER (Include area code) (937) 255-3636, ext 4507 (larry.burggraf@afit.edu)